

Rapid Conjugate Appearance of the Giant Ionospheric Lamb Wave in the Northern Hemisphere After Hunga-Tonga Volcano Eruptions

Jia-Ting Lin^{1,1}, P. K. Rajesh^{1,1}, Charles C. H. Lin^{1,1}, Min-Yang Chou^{2,2}, Jann-Yenq Liu^{3,3}, Jia Yue^{2,2}, Ho-Fang Tsai^{1,1}, Hoi-Man Chao^{1,1}, and Mu-Min Kung^{1,1}

¹National Cheng Kung University

²Goddard Space Flight Center

³National Central University

November 30, 2022

Abstract

The explosive eruption of the Hunga-Tonga volcano in the southwest Pacific at 0415UT on 15 January 2022 triggered gigantic atmospheric disturbances with surface air pressure wave propagating around the globe in Lamb mode. In space, concentric traveling ionosphere disturbances (CTIDs) are also observed as a manifestation of air pressure acoustic waves in New Zealand \sim 0500UT and Australia \sim 0630UT. As soon as the wave reached central Australia \sim 0800UT, CTIDs appeared simultaneously in the northern hemispheres through magnetic field line conjugate effect, which is much earlier than the arrival of the air pressure wave to Japan after 1100UT. Combining observations over Australia and Japan between 0800-1000UT, CTIDs with characteristics of phase velocities of 320-390 m/s are observed, matching with the dispersion relation of Lamb mode. The arrival of atmospheric Lamb wave to Japan later created in situ CTIDs showing the same Lamb mode characteristics as the earlier arriving CTIDs.

1 **Rapid Conjugate Appearance of the Giant Ionospheric Lamb Wave in the**
2 **Northern Hemisphere After Hunga-Tonga Volcano Eruptions.**

3

4 Jia-Ting Lin¹, Panthalingal K. Rajesh¹, Charles C. H. Lin¹, Min-Yang Chou^{2,3}, Jann-Yenq Liu^{4,5},
5 Jia Yue^{2,3}, Tung-Yuan Hsiao⁶, Ho-Fang Tsai¹, Hoi-Man Chao¹ and Mu-Min Kung¹

6

7 ¹Department of Earth Sciences, National Cheng Kung University, Tainan, Taiwan

8 ²NASA Goddard Space Flight Center, Community Coordinated Modeling Center, Greenbelt,
9 MD, USA

10 ³Physics Department, Catholic University of America, Washington, DC, USA

11 ⁴Center for Astronautical Physics and Engineering, National Central University, Taiwan

12 ⁵Department of Space Science and Engineer, National Central University, Taiwan

13 ⁶Nuclear Science and Technology Development Center, National Tsing Hua University, Hsinchu,
14 Taiwan

15 **Key points:**

- 16 1. Concentric traveling ionospheric disturbances (CTIDs) driven by volcano excited Lamb
17 wave are observed simultaneously in Australia and Japan.
- 18 2. Due to instantaneous magnetic field conjugate effect, the northern hemisphere CTIDs appear
19 3-hours prior to the arrival of surface Lamb wave
- 20 3. The CTIDs from conjugate hemispheres match with the theoretical dispersion relation of the
21 atmospheric Lamb mode.

22 **Abstract**

23 The explosive eruption of the Hunga-Tonga volcano in the southwest Pacific at 0415UT on
24 15 January 2022 triggered gigantic atmospheric disturbances with surface air pressure wave
25 propagating around the globe in Lamb mode. In space, concentric traveling ionosphere
26 disturbances (CTIDs) are also observed as a manifestation of air pressure acoustic waves in New
27 Zealand ~0500UT and Australia ~0630UT. As soon as the wave reached central Australia
28 ~0800UT, CTIDs appeared simultaneously in the northern hemispheres through magnetic field
29 line conjugate effect, which is much earlier than the arrival of the air pressure wave to Japan
30 after 1100UT. Combining observations over Australia and Japan between 0800-1000UT, CTIDs
31 with characteristics of phase velocities of 320-390 m/s are observed, matching with the
32 dispersion relation of Lamb mode. The arrival of atmospheric Lamb wave to Japan later created
33 in situ CTIDs showing the same Lamb mode characteristics as the earlier arriving CTIDs.

34 **Plain Language Summary**

35 The Hunga-Tonga Volcano eruption on 15 January 2022 has created the impulsive Lamb
36 wave propagation on the surface air pressure that has been observed globally. The Lamb wave,
37 typically moving at the sound speed of ~ 340 m/s, traveled 6 hours to reach Japan, but the Lamb
38 wave signature in the Earth's ionosphere, the ionized component of the atmosphere, arrived 3-
39 hours earlier than expected, thanks to the property of the ionospheric plasma being controlled by
40 the Earth's magnetic field. As soon as the surface Lamb wave reached Australia, the ionosphere
41 above showed concentric wave shape of the traveling ionospheric disturbances (TIDs) and the
42 effect was mapped to the northern hemisphere through the conductive magnetic field lines. This
43 is the first time such concentric waves from a volcanic eruption is observed simultaneously in
44 both the hemispheres. The much faster transmission of the ionosphere disturbances to the
45 northern hemisphere through the magnetic field lines is beyond expectations. Monitoring the
46 ionospheric disturbances could be a powerful early warning tool for the diagnosis of such
47 explosive events on the planet Earth.

48 **1. Introduction**

49 Although constrained along the magnetic field lines with gyro-motions, the plasma
50 distribution in the ionosphere, the ionized component of the Earth's atmosphere, could be
51 affected by perturbations in the neutral atmosphere through momentum transfer by ion-neutral
52 collisions (e.g. Heki and Ping, 2005), or through polarization electric field perpendicular to
53 magnetic field that drives $\delta E \times B$ electromagnetic drift across field lines (e.g. Chou et al., 2017a),
54 given that neutrals are abundant than ions at the ionospheric altitudes. Thus, neutral atmospheric
55 perturbations could be seen through the observations such as ionospheric total electron content
56 (TEC), and one of the signature forms of this coupling is the generation of traveling ionospheric
57 disturbances (TIDs). Such TIDs with shock acoustic characteristics occurred after rocket
58 launches accompanied by atmospheric perturbations (Lin et al., 2014; 2017a; Chou et al., 2018a).
59 Concentric TIDs (CTIDs), the feature of the concentric gravity wave effect to the ionosphere, are
60 observed associated with extreme weather systems in the lower atmosphere (e.g. Nishioka et al.,
61 2013; Chou et al., 2017b). There are events that created a broad spectrum of perturbations in
62 both acoustic and gravity wave modes, e.g., rocket launches that produce shock-acoustic waves
63 followed by concentric gravity waves (Lin et al., 2017b) or thermospheric ducted gravity waves
64 (Chou et al., 2018b). An extreme case is the 2011 Tohoku earthquake and tsunami which
65 triggered a diverse spectra of TIDs, including phase velocities of the high-speed Rayleigh wave
66 mode of ~ 3.5 km/s, acoustic mode of 1-1.2 km/s, gravity mode of ~ 300 -590 m/s and tsunami
67 mode of ~ 200 -250 m/s (e.g. Chen et al., 2011; Liu et al., 2011a; Rolland et al., 2011; Saito et al.,
68 2011; Tsugawa et al., 2011; Galvan et al., 2012; Azeem et al., 2017; Chou et al., 2020).

69 Additionally, explosive volcano events that release elevated plume to the atmosphere could
70 also produce TIDs (e.g. Heki, 2006), and most of the reported perturbations fall within the shock

71 and acoustic mode with frequencies of ~4-6 mHz. Shults et al. (2016) show that the eruption of
72 the Calbuco volcano on 22-23 April 2015 generated acoustic wave in the ionosphere with the
73 phase velocities of 900-1200 m/s. They also listed three other volcano events showing similar
74 phase velocity in the acoustic wave domain (Heki, 2006; Dautermann et al., 2009a, 2009b;
75 Nakashima et al., 2016). Nakashima et al. (2016) show TEC oscillations with frequencies of 3.7,
76 4.8 and 6.8 mHz, which are similar to the 4-6 mHz oscillations reported by Shults et al. (2016).
77 While these ionospheric perturbations in the acoustic mode reported in the above events were
78 limited within about 1000 km of the volcano source (Shults et al., 2016), one of the most
79 significant events that induced global atmosphere responses was the eruption of St. Helen on 18
80 May 1980. Liu et al. (1982) showed that the eruption of St. Helen created atmospheric pressure
81 disturbance waves and TIDs in the ionosphere worldwide. Their observations of TIDs could only
82 be explained by the propagation of the atmospheric Lamb wave modes with horizontal phase
83 velocity at the sound speed of ~310 m/s, with period ranging within 5-50 min.

84 Similar to the impacts reported during the St. Helen event, the recent Hunga Tonga - Hunga
85 Ha'apai volcano eruption on 15 January 2022, sent out bouts of shock waves rippling through the
86 air, literally making the entire atmosphere to vibrate. The breathtaking images of the event
87 captured by Earth observing satellites show Lamb waves circulating the Earth, with worldwide
88 ground weather stations recording multiple passages of the air pressure waves (Duncombe, 2022).
89 The atmospheric disturbances from this violent eruption triggered a plethora of wave
90 perturbations, impacting the ocean surfaces and creating atmospheric oscillations, including
91 acoustic and gravity waves (e.g. Adam, 2022) that could potentially modulate the electron
92 content in the ionosphere. The TEC observations show CTID's reaching several thousands of
93 kilometers away from the eruption source. Taking advantage of the dense Global Navigation

94 Satellite System (GNSS) receiver network over New Zealand, Australia, and Japan, we image
95 the Lamb wave perturbations in the ionosphere displaying CTIDs over Japan at least 3-hours
96 ahead of the expected arrival of the disturbances based on the estimates of the air pressure wave
97 propagation (according to the manuscript submitted at scientific online letters by Sekizawa and
98 Kohyama 2022; <https://doi.org/10.31223/X55K8V>, hereinafter referred to as Sekizawa and
99 Kohyama, 2022). This shows intriguing coupling from the magnetic conjugate regions in the
100 southern hemisphere. Chou et al. (2022) recently showed conjugate signatures of medium scale
101 traveling ionosphere disturbances (MSTID) produced by the tsunami propagation during the
102 2011 Tohoku earthquake. However, this is the first time such conjugate behavior of ionosphere
103 dynamo in coupling the polarization electric fields associated with concentric gravity waves
104 produced by the atmospheric perturbations from a volcanic eruption is observed. The wave
105 characteristics of the observed CTIDs and their conjugate appearances are discussed.

106

107 **2. GNSS TEC Observations**

108 The Hunga Tonga - Hunga Ha'apai islands (20.5S, 175.8 E) are rightly placed in the
109 proximity of the GNSS network maintained by Geological hazard information for New Zealand
110 and Geoscience Australia, offering the opportunity to examine the near field impact from the
111 volcanic eruption. Both the services combined adds up to about 600 GNSS receivers, receiving
112 signals from Global Positioning System (GPS) and GLObal Navigation Satellite System
113 (GLONASS) satellites. In addition, data from about 1300 stations of the GNSS network of the
114 Geospatial Information Authority of Japan and 140 stations of Central Weather Bureau of
115 Taiwan (Shin et al., 2011; 2013) are also used. Such dense networks, though limited to certain
116 regions, enables rapid examination of TEC variations with high spatial and temporal resolutions.

117 The information about the data sources is given in the Open Research section. The 30-second
118 sampled GNSS observations are used to derive vertical TEC at a sub-ionospheric altitude of 300
119 km, with a low elevation cut-off of 20° . The TEC variations are extracted by applying
120 Butterworth bandpass filters of 12-20 mins and 30-50 min to better present the small- and large-
121 scale atmospheric waves associated with the volcanic eruption before distributing to their
122 geolocations of the sub-ionospheric points (SIPs).

123 Figure 1 shows the time evolution of the filtered TEC maps for periods within 30-50 mins
124 and 12-20 mins at 0647, 0853, 0926 and 1120 UT. The filtered TECs projected to the conjugated
125 hemisphere using magnetic apex coordinates (Richmond, 1995; Emmert et al., 2010) are also
126 shown using different colormaps. Overplotted red dashed circles indicate the atmospheric
127 disturbances, mostly the Lamb wave, traveling at the speed of sound calculated using
128 temperature from NCEP reanalysis (Kalnay et al., 1998) and mean molecular mass from the
129 empirical NRLMSISE-00 model (Picone et al., 2002). According to Sekizawa and Kohyama
130 (2022), the arrival of the air pressure disturbances at Japan is ~ 1100 UT and the estimation
131 indicated by the dashed circles matches the arrival time. Liu et al. (1982) show from their model
132 calculation that the TIDs of acoustic-gravity waves associated with lamb modes are ~ 5 -50 mins
133 and we, therefore, focus on the TEC oscillations within these time periods. The bandpass
134 filtering is performed at 12-20 min (hereinafter referred as 12-20 wave) to illustrate the finer
135 structure of the CTIDs and at 30-50 min (hereinafter referred as 30-50 wave) to show the larger
136 scale CTIDs. The movie of the time evolutions of bandpass filtering of 12-20, 30-50 and 10-60
137 mins are provided in the supplementary material (Movie S1). In Figure 1 and movie S1, CTIDs
138 of both bands are seen clearly over New Zealand and Australia area after 0647UT and become
139 prominent and clearly conjugated, either mapping the Australia TECs to the northern hemisphere

140 or mapping the Japan TECs to the southern hemisphere after 0800UT. Thirty minutes ahead of
141 the arrival of the surface pressure wave in Japan, around 1030 UT, the propagation direction of
142 CTIDs in Japan started to turn from westward to north-westward, aligning perpendicular to the
143 wavefront of the surface waves. The 12-20 waves start to show direction change of the wavefront
144 ~1045UT, lagging ~15 minutes behind the 30-50 waves. The clear conjugated waves are still
145 seen in the southern hemisphere for the 12-20 wave after 1100UT upon the direct arrival of the
146 surface wave to Japan.

147 The spectral analysis of the GNSS TEC from both Australia and Japan has been performed
148 for oscillations of periods shorter than 1 h by using Hilbert-Huang transform (HHT, cf. Huang et
149 al., 1998; Liu et al., 2011b). Note that only TEC observations over the conjugate area (130-
150 140°E) are used to investigate the ionospheric conjugacy of CTIDs. Figure 2 shows the Hilbert
151 spectrum of TECs from both Australia and Japan. The amplitudes of both Hilbert spectra start to
152 intensify coherently ~0700UT and become prominent around 0800-1000UT, peaking at
153 ~0900UT for both regions for periods greater than 10 mins. Generally, the amplitude
154 intensifications occur after 0700UT for both spectra in the frequency range ~0.25-2 mHz or
155 period of 8-60 min, which is consistent with the 5-50 mins period suggested by Liu et al. (1982).

156 Figure 3 illustrate the keograms of the filtered TECs of New Zealand and Australia (Figs. 3a,
157 c) and Japan (Fig. 3b, d). As the filtered TECs over Japan are mapped to the southern hemisphere,
158 the distances to the volcano are counted from their southern hemisphere magnetic conjugate
159 locations. Figure 3a shows, for the 30-50 min period, that the first prominent packet of TIDs
160 appears clearly over New Zealand (distances < 3000 km) around 0500-0700UT. The second
161 prominent packet appears over Australia ~0700-1000UT. The 12-20 waves (Fig. 3c) lag behind

162 30-50 waves for at least 15 min or even longer. Clear conjugate effects for the two periods are
163 seen in the TIDs over Japan after 0730UT (Figs. 3c and 3d).

164 Except TID#NZ1, which shows phase velocity exceeding 500 m/s, most of the TIDs have
165 phase velocities of 320-390 m/s, and periods of ~40 mins for the 30-50 waves and 15-18 mins
166 for the 12-20 waves. These wave characteristics are further applied to estimate the dispersion
167 relation using Equation (1) (cf. Hines, 1960) expressed as follows. The equation is also utilized
168 to calculate the dispersion curves of acoustic and gravity modes.

$$169 \quad m^2 = \left(1 - \frac{\omega_a^2}{\omega^2}\right) \frac{\omega^2}{c_0^2} - k^2 \left(1 - \frac{\omega_b^2}{\omega^2}\right) \quad (1)$$

170 where m is the complex vertical wave number, $\omega_a = \sqrt{\frac{\gamma g}{4H} + \frac{g}{T} \frac{dT}{dz}}$ is acoustic cutoff frequency,

171 $\omega_b = \sqrt{\frac{(\gamma-1)g}{\gamma H} + \frac{g}{T} \frac{dT}{dz}}$ is buoyancy frequency, $\omega = k(c_h - u)$ is intrinsic frequency, u is the

172 neutral wind speed in the direction of wave propagation, c_h is the horizontal phase velocity, H is

173 the scale height, γ is the ratio of specific heats, g is the gravitational acceleration, and T is neutral

174 temperature. These parameters are adopted from empirical neutral atmospheric parameters from

175 the Horizontal Wind Model 2014 (Drob et al., 2015) and NRLMSISE-00. The acoustic-gravity

176 wave is evanescent or freely propagating while $m^2 < 0$ or $m^2 > 0$. We identify the characteristic of

177 these TIDs by calculating the dispersion curves for Figure 4 ($m^2 = 0$) using equation (1) (cf. Yeh

178 and Liu, 1974; Matsumura et al., 2012). The black solid, dashed, dashed-dot and dotted lines

179 indicate the dispersion curves of gravity mode and acoustic mode at 300, 250, 200 and 150 km

180 altitude, respectively. The colored dots indicate the calculated intrinsic frequencies of observed

181 TIDs indicated in Figure 3. The Lamb wave mode with constant phase velocity of sound is added

182 with the blue solid line in Figure 4. It is seen that the color dots of TIDs are aligned along the
183 blue solid line indicating the Lamb wave signature of CTIDs observed in this study.

184 Since atmospheric Lamb wave has non-dispersive characteristics as acoustic waves (Francis,
185 1973), it is expected to see similar wave characteristics of CTIDs over Japan after the actual
186 arrival of the Lamb wave to Japan ~1100UT. Figure S2 shows the 30-50 and 12-20 waves over
187 Japan ~1000-1400UT. It indicates that the 30-50 waves again lead the 12-20 wave, and these
188 waves generally fit along the curve of Lamb mode, except the early appearance of 12-20 waves
189 (TID#JP6, JP7 and JP8).

190

191 **3. Discussions and Conclusion**

192 We present the first clear images of CTIDs propagating with the Lamb mode driven by the
193 volcano excited Lamb wave for the first time (Fig. 1). Taking advantage of the magnetic
194 conjugate effect by combining observations from Australia and Japan, a comprehensive picture
195 of concentric waves could be drawn, and their wave characteristics are all consistent with the
196 dispersion relation of Lamb mode as shown in Figs. 3 and 4. Another important discovery is that
197 the CTIDs could be seen conjugately even during daytime (Dusk), which was not previously
198 reported in the literature. This new finding suggests that the Lamb wave excited by the explosive
199 Hunga Tonga - Hunga Ha'apai volcano could affect the global ionosphere much sooner than
200 expected as the driven CTIDs are capable of being transmitted to the magnetically conjugate
201 hemispheres.

202 During the geomagnetically quiescent period, the magnetic conjugate effect of the
203 ionosphere is well known and there are studies on the conjugate effect of plasma instabilities
204 during nighttime, such as equatorial plasma bubble (EPB) and MSTID (e.g. Otsuka et al., 2004;

205 Fukushima et al., 2015; Valladares and R. Sheehan, 2016). During daytime the conjugate effect
206 is believed to be rare because the efficiency of electric field mapping is proportional to the ratio
207 of field line integration of the Pedersen conductivities in F- and E-regions as $\frac{\Sigma_p^F}{\Sigma_p^F + \Sigma_p^E}$. The much
208 higher E-region conductivity during daytime then prevents the electric field mapping in the F-
209 region. However, some exceptions were observed by Jonah et al. (2017) and they adopted the
210 explanation given by Abdu et al. (2015) that during the late afternoon approaching the sunset
211 hours, the ratio of F- and E-region conductivities could be close to 0.8 or greater making electric
212 field mapping likely to happen. Our observation of the Lamb wave driven CTIDs in Japan
213 appeared after 0730UT or 1630LT, close to the time-period when the mapping is likely favored.

214 The 2011 Great Tohoku earthquake and tsunami also triggered conjugate effect of the
215 tsunami driven gravity waves, but they were mainly during nighttime. Huba et al. (2015)
216 simulated the conjugate ionospheric effects associated with the tsunami-driven gravity waves
217 using self-consistent electrodynamics and suggested that the perpendicular neutral wind
218 perturbation could induce polarization electric fields mapping along the geomagnetic field line to
219 the conjugate southern hemisphere of Hawaii. Their simulations were compared with the sparse
220 GPS-derived TEC when the tsunami passed by Hawaii during nighttime. Chou et al. (2022)
221 discovered that the reflected tsunami was able to drive gravity waves over Japan and triggered
222 prominent MSTID occurring in March, a season of rare MSTID occurrence, and further mapped
223 to the conjugate southern hemisphere over Australia. However, the initial main TIDs driven by
224 the earthquake and tsunami did not produce any conjugate effect, and the coupled gravity wave-
225 Perkins instability may contribute to the interhemispheric conjugate process due to the specific
226 wavefront alignment of the MSTIDs. This study, therefore, provides direct observational

227 evidence to support that wind-dynamo coupling (e.g., Huba et al., 2015) alone is sufficient to
228 induce the conjugate effect.

229 Surface air pressure wave traveling with Lamb mode occurred during previous explosion
230 events, e.g. Kratatoa volcano eruption in 1883 (Pekeries, 1939), Tunguska event in Siberia 1908
231 (Whippe, 1930) and St. Helen eruption in 1980 (Liu et al., 1980). According to Francis (1973),
232 the lower atmosphere Lamb wave could propagate long distances with little dissipation and its
233 attenuation distance, defined by attenuation by a factor of $1/e$, is of the order of Earth's
234 circumference or greater. The non-dispersive and weak attenuation properties of the air pressure
235 wave (Duncombe, 2022) again suggest that it is the Lamb wave traveling globally, excited by the
236 volcano eruption, being studied here. The ionosphere disturbances also show weak attenuation
237 feature. The amplitudes of the CTIDs (percentage of TEC perturbations) over New Zealand-
238 Australia around 0500-1000UT (Figs. 3a and 3b) and Japan, more than 8000 km away from the
239 volcano, around 1000-1300UT, are comparable (Fig S2), indicating the weak attenuation nature
240 of the Lamb wave. Although the Lamb wave generally travels in the troposphere and
241 stratosphere below about 30 km altitude and its energy decreases with altitudes, the exponential
242 decrease of neutral density with increasing altitude actually increases its amplitude. Additionally,
243 Nishida et al. (2014) show that Lamb wave could theoretically exist at thermosphere altitudes.
244 Our observations of CTIDs agree with the dispersion relation of Lamb mode and the weak
245 attenuation suggests that the CTIDs driven by the Hunga-Tonga volcano have Lamb wave
246 characteristics.

247 It is worthwhile to note that (according to Fig. 1 and Movie S1), prior to the arrival of the air
248 pressure Lamb wave to Australia, there are already signatures of TIDs. By comparing with the
249 intense tsunami effect of the 2011 Tohoku earthquake, there were leading TIDs ahead of the

250 tsunami arrival (e.g. Makela et al., 2011). Inchin et al. (2020) suggest that the tsunami-induced
251 gravity wave spectrum has phase variations from long-period phases at the head of the packet to
252 short-period phases at its tail. A similar process might occur in this event, where, instead of the
253 tsunami exciting the gravity waves the surface Lamb wave might excite a broad spectrum of
254 gravity waves. Gravity waves with longer period waves travel faster than short period waves
255 (Figs. 1, 3, S2). Gravity waves with the period locked to the dominant period of Lamb mode will
256 eventually travel at the same speed of surface pressure wave after reaching the ionosphere and
257 the surface pressure Lamb wave plays the role of continuously triggering gravity wave as a
258 moving source. This process is also similar to the seismic Rayleigh wave that continuously
259 excites seismo-TIDs with the same periods and speeds (e.g., Liu et al., 2011a).

260 Rakoto et al. (2017) developed the ocean-atmosphere coupled model for tsunami effects
261 with analyses of acoustic, gravity, tsunami and Lamb modes. They find that the tsunami mode
262 does not transfer energy to the Lamb mode through resonance as their frequency branches are
263 not crossing each other. On the other hand, the tsunami mode could excite gravity waves due to
264 the crossing frequency branches of the tsunami and gravity modes. Similarly, for the volcano
265 effect discussed here, the Lamb mode frequency crosses through the frequencies of gravity
266 modes (Figs. 4 and S3) and it is likely that the Lamb wave could thereby induce a packet of
267 gravity waves. The lagged 12-20 waves in Fig. 1 and the keograms of Figs. 3 and S2 showing the
268 smaller scale waves appearing at later times suggest that such a process might be operational.

269 It is noted that there was a minor magnetic storm during the volcano eruption, with the
270 disturbance storm index (Dst) dropping to about -94 nT at ~2300 UT on 14 January 2022.
271 Magnetic storms are known to generate large-scale TIDs (LSTIDs) that propagate equatorward
272 (e.g., Richmond, 1978), and could give rise to TEC perturbations (Cherniak and Zakharenkova,

273 2018). However, the storm influence could be ruled out here to have any role in producing the
274 TEC observed fluctuations after the eruption. Though interplanetary magnetic field (IMF Bz)
275 turned southward after 1800 UT on this day, gradually reaching about -18 nT by 2230 UT, the
276 solar wind velocity was only 350-380 km/s during this period and the proton density did not
277 increase much, suggesting only minor storm impact. The auroral electrojet (AE) index, which
278 briefly reached over 1000 during 2100-2200 UT, and again spiked for a few minutes before 2300
279 UT on 01/14 when IMF Bz was southward, returned to values below 500 before 0000 UT on
280 01/15 and subsequently remained subdued, further indicating lack of any significant high latitude
281 activity. The IMF Bz also turned northward by 2330 UT on 01/14, and later revealed fluctuations
282 typical of CIR events. The Dst index further shows that by the time the eruption occurred, the
283 storm was well into the recovery phase. Moreover, LSTIDs usually propagate equatorward from
284 high latitudes, whereas the observed perturbations show CTIDs expanding poleward as the Lamb
285 waves circulated the Earth.

286 In conclusion, we present the first comprehensive picture of the concentric traveling
287 ionospheric disturbances in conjugate hemispheres coherently showing the Lamb wave
288 characteristic driven by the powerful eruption of Hunga Tonga - Hunga Ha'apai. The varying
289 phase velocities of the ionospheric disturbances with different wave periods suggest that the
290 Lamb waves excite a broad spectra of gravity waves, further indicating resonant wave-coupling
291 of co-existing Lamb and gravity modes. The conductive geomagnetic field lines enable the rapid
292 transmission of disturbance waves to the northern hemisphere on Alfvénic timescales (~300
293 km/s), leading to rapid electrified ionospheric disturbances faster than the direct Lamb waves
294 over Japan, which is beyond expectations. The GNSS networks therefore could be a powerful

295 tool for early warning system for the diagnosis of such explosive events on the planet Earth, and
296 advance our understanding of how natural hazards drive space weather.

297

298

299 **Acknowledgements**

300 This work is partly supported by the Ministry of Science and Technology under MOST 110-
301 2111-M-006-004 and MOST 110-2119-M-006-001. MYC was supported by NASA grant
302 80NSSC20K0628. CHL wishes to thank Chao-Han Liu for useful discussions. The authors
303 acknowledge the Geological hazard information for New Zealand, the Geoscience Australia, the
304 Geospatial Information Authority of Japan, the Central Weather Bureau, Taiwan for managing
305 the GNSS observations, and the Geomagnetic Data Service of Kyoto University and NOAA
306 Space Weather Prediction Center for geomagnetic and solar wind parameters.

307

308 **Open Research**

309 The GNSS RINEX data are available from the Geological hazard information for New Zealand
310 (GeoNet, <https://www.geonet.org.nz/data/types/geodetic>), the Geoscience Australia GNSS data
311 archive (<https://www.ga.gov.au/scientific-topics/positioning-navigation/geodesy/gnss-networks>),
312 the Geospatial Information Authority of Japan (GEONET,
313 https://www.gsi.go.jp/ENGLISH/geonet_english.html) and the Geophysical Database
314 Management System of Central Weather Bureau, Taiwan (<https://gdms.cwb.gov.tw/index.php>).
315 Dst and AE indices are available at the Geomagnetic Data Service of Kyoto University
316 (<http://wdc.kugi.kyoto-u.ac.jp/wdc/Sec3.html>) and the solar wind parameters could be accessed
317 from NOAA Space Weather Prediction Center (<https://www.swpc.noaa.gov/products/real-time->

318 solar-wind). The processed TEC data is available at
319 <https://doi.org/10.6084/m9.figshare.19115624>.

320

321 **Reference**

322 Abdu, M. A., J. R. de Souza, E. A. Kherani, I. S. Batista, J. W. MacDougall, and J. H. A. Sobral
323 (2015), Wave structure and polarization electric field development in the bottomside F
324 layer leading to postsunset equatorial spread F, *J. Geophys. Res. Space Physics*, 120,
325 6930–6940, doi:10.1002/2015JA021235.

326 Adam, D. (2022), Tonga volcano eruption created puzzling ripples in Earth’s atmosphere,
327 *Nature* **601**, 497.

328 Azeem, I., Vadas, S. L., Crowley, G., and Makela, J. J. (2017), Traveling ionospheric
329 disturbances over the United States induced by gravity waves from the 2011 Tohoku
330 tsunami and comparison with gravity wave dissipative theory, *J. Geophys. Res. Space*
331 *Physics*, 122, 3430– 3447, doi:10.1002/2016JA023659.

332 Chen, C. H., A. Saito, C. H. Lin, J. Y. Liu, H. F. Tsai, T. Tsugawa, Y. Otsuka, M. Nishioka and
333 M. Matsumura (2011), Long-distance propagation of ionospheric disturbance generated by
334 the 2011 Tohoku earthquake, *Earth Planets and Space*, 63, 7, 881-884,
335 doi:10.5047/eps.2011.06.026

336 Cherniak, I., and Zakharenkova, I. (2018). Large-scale traveling ionospheric disturbances origin
337 and propagation: Case study of the December 2015 geomagnetic storm. *Space Weather*, 16,
338 1377– 1395. <https://doi-org.cuucar.idm.oclc.org/10.1029/2018SW001869>

339 Chou, M. Y., C. H. Lin, J. Yue, L. C. Chang, H. F. Tsai and C. H. Chen (2017a), Medium-scale
340 traveling ionospheric disturbances triggered by Super Typhoon Nepartak (2016), *Geophys.*
341 *Res. Lett.*, 44, 7569–7577, doi:10.1002/2017GL073961

342 Chou, M. Y., C. H. Lin, J. Yue, H. F. Tsai, Y. Y. Sun, J. Y. Liu and C. H. Chen (2017b),
343 Concentric traveling ionosphere disturbances triggered by Super Typhoon Meranti (2016),
344 *Geophys. Res. Lett.*, 44, doi:10.1002/2016GL072205.

345 Chou, M. Y., M. H. Shen, C. H. Lin, J. Yue, C. H. Chen, J. Y. Liu and J. T. Lin (2018a),
346 Gigantic circular shock acoustic waves in the ionosphere triggered by the launch of
347 FORMOSAT-5 satellite, *Space Weather*, 16, 172-184, doi:10.1002/2017SW001738.

348 Chou, M.-Y., Lin, C. H., Shen, M.-H., Yue, J., Huba, J. D., & Chen, C.-H. (2018b), Ionospheric
349 disturbances triggered by SpaceX Falcon Heavy, *Geophysical Research*
350 *Letters*, 45, doi:10.1029/2018GL078088.

351 Chou, M.-Y., Cherniak, I., Lin, C. C. H., & Pedatella, N. M. (2020). The persistent ionospheric
352 responses over Japan after the impact of the 2011 Tohoku earthquake. *Space Weather*, 18,
353 e2019SW002302. <https://doi.org/10.1029/2019SW002302>

354 Chou, M.-Y., Yue, J., Lin, C. C. H., Rajesh, P. K., & Pedatella, N. M. (2022). Conjugate effect
355 of the 2011 Tohoku reflected tsunami-driven gravity waves in the ionosphere. *Geophysical*
356 *Research Letters*, 49, e2021GL097170, doi:10.1029/2021GL097170.

357 Dautermann, T., Calais, E., Lognonné, P., Mattioli, G.S., 2009a. Lithosphere– atmosphere–
358 ionosphere coupling after the 2003 explosive eruption of the Soufriere Hills Volcano,
359 Montserrat. *Geophys. J. Int.* 179 (3), 1537–1546.

360 Dautermann, T., Calais, E., Mattioli, G.S., 2009b. Global positioning system detection and
361 energy estimation of the ionospheric wave caused by the 13 July 2003 explosion of the

362 Soufrière Hills Volcano, Montserrat. *J. Geophys. Res.* 114 (B2), B02202.
363 doi:10.1029/2008JB005722.

364 Drob, D. P., Emmert, J. T., Meriwether, J. W., Makela, J. J., Doornbos, E., Conde, M., et al.
365 (2015). An update to the horizontal wind model (HWM):The quiet time thermosphere. *Earth*
366 *Space Science*, 2(7), 301–319. <https://doi.org/10.1002/2014EA000089>

367 Duncombe, J. (2022), The surprising reach of Tonga’s giant atmospheric waves, *Eos*, 103,
368 <https://doi.org/10.1029/2022EO220050>.

369 Emmert, J. T., A. D. Richmond, and D. P. Drob (2010), A computationally compact
370 representation of Magnetic-Apex and Quasi-Dipole coordinates with smooth base vectors,
371 *J. Geophys. Res.*, 115(A8), A08322, doi:10.1029/2010JA015326.

372 Francis, S. H. (1973), Acoustic-gravity modes and large-scale traveling ionospheric disturbances
373 of a realistic, dissipative atmosphere, *J. Geophys. Res.*, 78(13), 2278– 2301,
374 doi:[10.1029/JA078i013p02278](https://doi.org/10.1029/JA078i013p02278).

375 Fukushima, D., Shiokawa, K., Otsuka, Y., Nishioka, M., Kubota, M., Tsugawa, T., Nagatsuma,
376 T., Komonjinda, S., and Yatini, C. Y. (2015), Geomagnetically conjugate observation of
377 plasma bubbles and thermospheric neutral winds at low latitudes. *J. Geophys. Res. Space*
378 *Physics*, 120, 2222– 2231. doi: [10.1002/2014JA020398](https://doi.org/10.1002/2014JA020398).

379 Galvan, D. A., Komjathy, A., Hickey, M. P., Stephens, P., Snively, J., Tony Song, Y., Butala, M.
380 D., and Mannucci, A. J. (2012), Ionospheric signatures of Tohoku-Oki tsunami of March
381 11, 2011: Model comparisons near the epicenter, *Radio Sci.*, 47, RS4003,
382 doi:[10.1029/2012RS005023](https://doi.org/10.1029/2012RS005023).

383 Heki, K., and J. Ping (2005), Directivity and apparent velocity of the coseismic ionospheric
384 disturbances observed with a dense GPS array, *Earth Planet. Sci. Lett.*, 236, 845–855,
385 doi:10.1016/j.epsl.2005.06.010.

386 Heki, K. (2006), Explosion energy of the 2004 eruption of the Asama Volcano, central Japan,
387 inferred from ionospheric disturbances, *Geophys. Res. Lett.*, 33, L14303,
388 doi:10.1029/2006GL026249.

389 Hines, C. O. (1960), Internal atmospheric gravity waves at ionospheric heights, *Can. J. Phys.*, 38,
390 1441.

391 Huang, N. E., et al. (1998), The empirical mode decomposition and the Hilbert spectrum for
392 nonlinear and nonstationary time series analysis, *Proc. R. Soc. London, Ser. A*, 454, 903–
393 995, doi:10.1098/rspa.1998.0193.

394 Huba, J. D., G. Joyce, and J. Krall (2008), Three-dimensional equatorial spread F modeling,
395 *Geophys. Res. Lett.*, 35, L10102, doi:10.1029/2008GL033509.

396 Huba, J. D., D. P. Drob, T.-W. Wu, and J. J. Makela (2015), Modeling the ionospheric impact of
397 tsunami-driven gravity waves with SAMI3: Conjugate effects, *Geophys. Res. Lett.*, 42,
398 5719–5726, doi:10.1002/2015GL064871.

399 Inchin, P. A., Heale, C. J., Snively, J. B., & Zettergren, M. D. (2020). The dynamics of nonlinear
400 atmospheric acoustic-gravity waves generated by tsunamis over realistic bathymetry.
401 *Journal of Geophysical Research: Space Physics*, 125, e2020JA028309.
402 <https://doi.org/10.1029/2020JA028309>

403 Jonah, O. F., E. A. Kherani, and E. R. De Paula (2017), Investigations of conjugate MSTIDS
404 over the Brazilian sector during daytime, *J. Geophys. Res. Space Physics*, 122, 9576–9587,
405 doi:10.1002/2017JA024365.

406 Kalnay, E., Kanamitsu, M., Kistler, R., Collins, W., Deaven, D., Gandin, L., Iredell, M., Saha,
407 S., White, G., Woollen, J., Zhu, Y., Chelliah, M., Ebisuzaki, W., Higgins, W., Janowiak, J.,
408 Mo, K. C., Ropelewski, C., Wang, J., Leetmaa, A., Reynolds, R., Jenne, R., & Joseph, D.
409 (1996). The NCEP/NCAR 40-Year Reanalysis Project, *Bulletin of the American*
410 *Meteorological Society*, 77(3), 437-472. Retrieved Feb 6, 2022, from
411 [https://journals.ametsoc.org/view/journals/bams/77/3/1520-](https://journals.ametsoc.org/view/journals/bams/77/3/1520-0477_1996_077_0437_tnyrp_2_0_co_2.xml)
412 [0477_1996_077_0437_tnyrp_2_0_co_2.xml](https://journals.ametsoc.org/view/journals/bams/77/3/1520-0477_1996_077_0437_tnyrp_2_0_co_2.xml)

413 Lin, C. H., Lin, J. T. Lin, C. H. Chen, M. Matsumura, J. Y. Liu, Y. Y. Sun, W. H. Chen, Y.
414 Kakinami, H. Liu, and R. J. Rau (2014), Ionospheric Shock Waves Triggered by Rockets,
415 *Ann. Geophys.*, 32, 9, 1145–1152, doi:10.5194/angeo-32-1145-2014

416 Lin, C. H. , C. H. Chen, M. Matsumura, J.-T. Lin and Y. Kakinami (2017a), Observation and
417 simulation of the ionospheric disturbance waves triggered by rocket exhausts, *J. Geophys.*
418 *Res. Space Physics*, 122, doi:10.1002/2017JA023951.

419 Lin, C. H., M. H. Shen, M. Y. Chou, C. H. Chen, J. Yue, P. C. Chen, and M. Matsumura (2017b),
420 Concentric traveling ionospheric disturbances triggered by the launch of a SpaceX Falcon
421 9 rocket, *Geophys. Res. Lett.*, 44, 7578–7586, doi:10.1002/2017GL074192.

422 Liu, C. H., et al. (1982), Global dynamic responses of the atmosphere to the eruption of Mount
423 St. Helens on May 18, 1980, *J. Geophys. Res.*, 87(A8), 6281– 6290,
424 doi:[10.1029/JA087iA08p06281](https://doi.org/10.1029/JA087iA08p06281).

425 Liu, J.-Y., C.-H. Chen, C.-H. Lin, H.-F. Tsai, C.-H. Chen, and M. Kamogawa (2011a),
426 Ionospheric disturbances triggered by the 11 March 2011 M9.0 Tohoku earthquake, *J.*
427 *Geophys. Res.*, 116, A06319, doi:10.1029/2011JA016761.

428 Liu, J. Y., Y. Y. Sun, Y. Kakinami, C. H. Chen, C. H. Lin, and H. F. Tsai (2011b), Bow and
429 stern waves triggered by the Moon's shadow boat, *Geophys. Res. Lett.*, 38, L17109,
430 doi:10.1029/2011GL048805.

431 Makela, J. J., et al. (2011), Imaging and modeling the ionospheric airglow response over Hawaii
432 to the tsunami generated by the Tohoku earthquake of 11 March 2011, *Geophys. Res. Lett.*,
433 38, L00G02, doi:10.1029/2011GL047860.

434 Matsumura, M., H. Shinagawa, and T. Iyemori (2012), Horizontal extension of acoustic
435 resonance between the ground and the lower thermosphere, *J. Atmos. Sol. Terr. Phys.*, 75-76,
436 127–132.

437 Nakashima, Y., K. Heki, A. Takeo, M. N. Cahyadi, A. Aditiya, and K. Yoshizawa (2016),
438 Atmospheric resonant oscillations by the 2014 eruption of the Kelud volcano, Indonesia,
439 observed with the ionospheric total electron contents and seismic signals, *Earth Planet. Sci.*
440 *Lett.*, 434, 112–116, doi:10.1016/j.epsl.2015.11.029.

441 Nishida, K., N. Kobayashi and Y. Fukao (2014), Background Lamb waves in the Earth's
442 atmosphere, *Geophys. J. Int.*, 196, 312–316, doi: 10.1093/gji/ggt413

443 Otsuka, Y., K. Shiokawa, T. Ogawa, and P. Wilkinson (2004), Geomagnetic conjugate
444 observations of medium-scale traveling ionospheric disturbances at midlatitude using all-
445 sky airglow imagers, *Geophys. Res. Lett.*, 31, L15803, doi:10.1029/2004GL020262.

446 Pekeris, C. L. (1939), The propagation of a pulse in the atmosphere, *Proc. R. Soc. London Ser. A*,
447 A171, 434-449.

448 Picone, J. M., A. E. Hedin, D. P. Drob, and A. C. Aikin (2002), NRLMSISE-00 empirical model
449 of the atmosphere: Statistical comparisons and scientific issues, *J. Geophys. Res.*, 107
450 (A12), 1468, doi:10.1029/2002JA009430.

451 Rakoto, V., P. Lognonné, L. Rolland (2017), Tsunami modeling with solid Earth–ocean–
452 atmosphere coupled normal modes, *Geophysical Journal International*, Oxford University
453 Press (OUP), 2017, 211 (2), pp.1119 - 1138. 10.1093/gji/ggx322 . hal-01737686

454 Richmond, A. D. (1978), Gravity wave generation, propagation, and dissipation in the
455 thermosphere, *J. Geophys. Res.*, 83(A9), 4131– 4145, doi:10.1029/JA083iA09p04131.

456 Richmond, A. D., Ionospheric electrodynamics using Magnetic Apex Coordinates, *J. Geomagn.*
457 *Geoelectr.*, 47, 191–212, 1995.

458 Rolland, L.M., Lognonné, P., Astafyeva, E. *et al.* The resonant response of the ionosphere
459 imaged after the 2011 off the Pacific coast of Tohoku Earthquake. *Earth Planet Sp* **63**, 62
460 (2011). <https://doi.org/10.5047/eps.2011.06.020>

461 Saito, A., Tsugawa, T., Otsuka, Y., Nishioka, M., Iyemori, T., Matsumura, M., Saito, S., Chen,
462 C.H., Goi, Y., Choosakul, N., 2011. Acoustic resonance and plasma de- pletion detected by
463 GPS total electron content observation after the 2011 off the Pacific coast of Tohoku
464 Earthquake. *Earth Planets Space* 63 (7), 863–867, doi:10.5047/eps.2011.06.034.

465 Shin, T. C., K. W. Kuo, P. L. Leu, C. H. Tsai, and J. S. Jiang, 2011: Continuous CWB GPS array
466 in Taiwan and applications to monitoring seismic activity. *Terr. Atmos. Ocean. Sci.*, 22,
467 521-533, doi: 10.3319/TAO.2011.05.18.01(T)

468 Shin, T. C., C. H. Chang, H. C. Pu*, H. W. Lin, and P. L. Leu, 2013: The Geophysical Database
469 Management System in Taiwan. *Terr. Atmos. Ocean. Sci.*, 24, 11-18, doi:
470 10.3319/TAO.2012.09.20.01(T)

471 Shults, K., E. Astafyeva, and S. Adourian (2016), Ionospheric detection and localization of
472 volcano eruptions on the example of the April 2015 Calbuco events, *J. Geophys. Res.*
473 *Space Physics*, 121, 10,303–10,315, doi:10.1002/2016JA023382.)

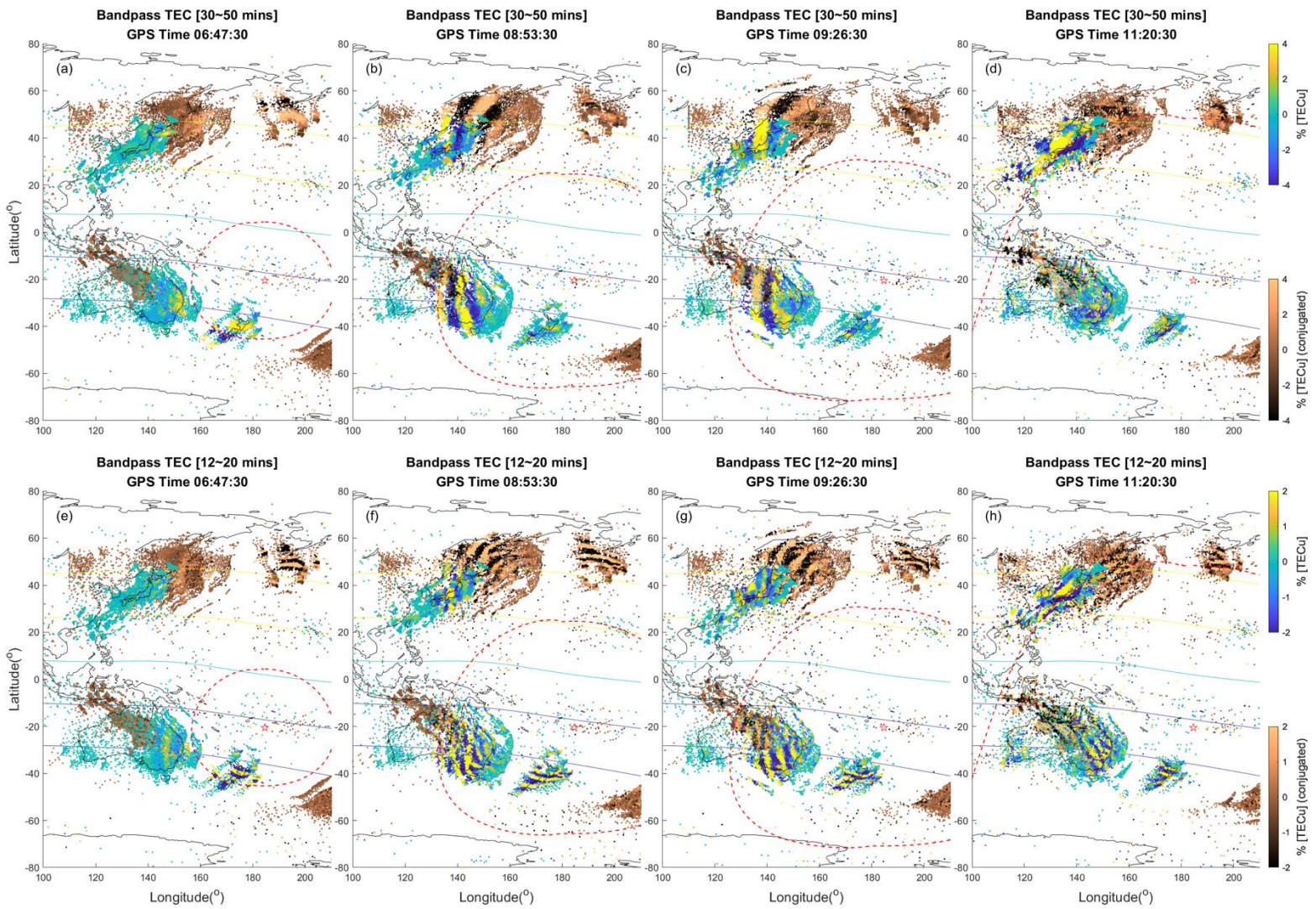
474 Tsugawa, T., A. Saito, Y. Otsuka, M. Nishioka, T. Maruyama, H. Kato, T. Nagatsuma, and K. T.
475 Murata, Ionospheric disturbances detected by GPS total electron content observation after
476 the 2011 off the Pacific coast of Tohoku Earthquake, *Earth Planets Space*, **63**, this issue,
477 875–879, 2011.

478 Valladares, C. E., and R. Sheehan (2016), Observations of conjugate MSTIDs using networks of
479 GPS receivers in the American sector, *Radio Sci.*, 51, 1470–1488,
480 doi:10.1002/2016RS005967.

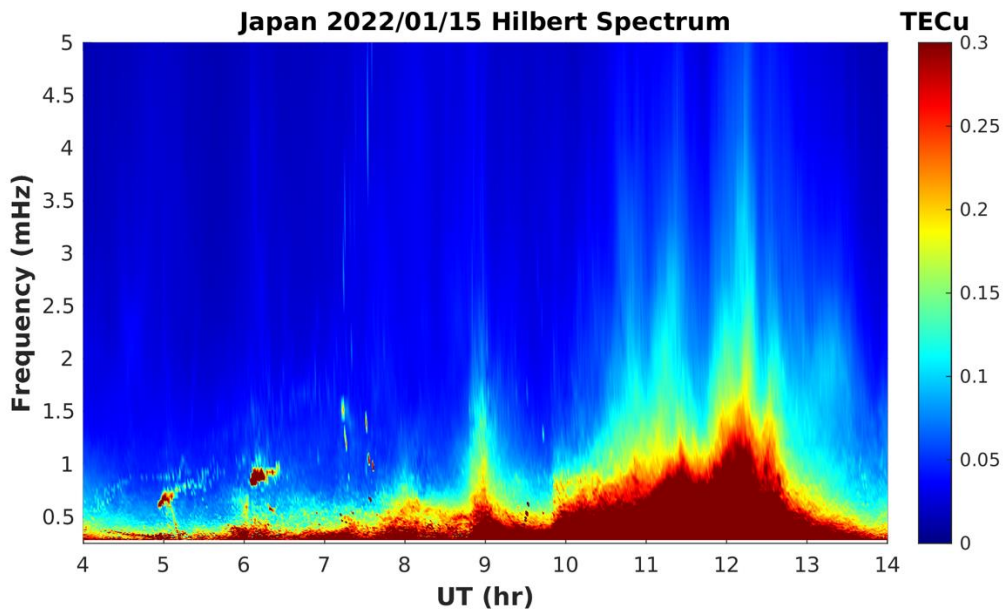
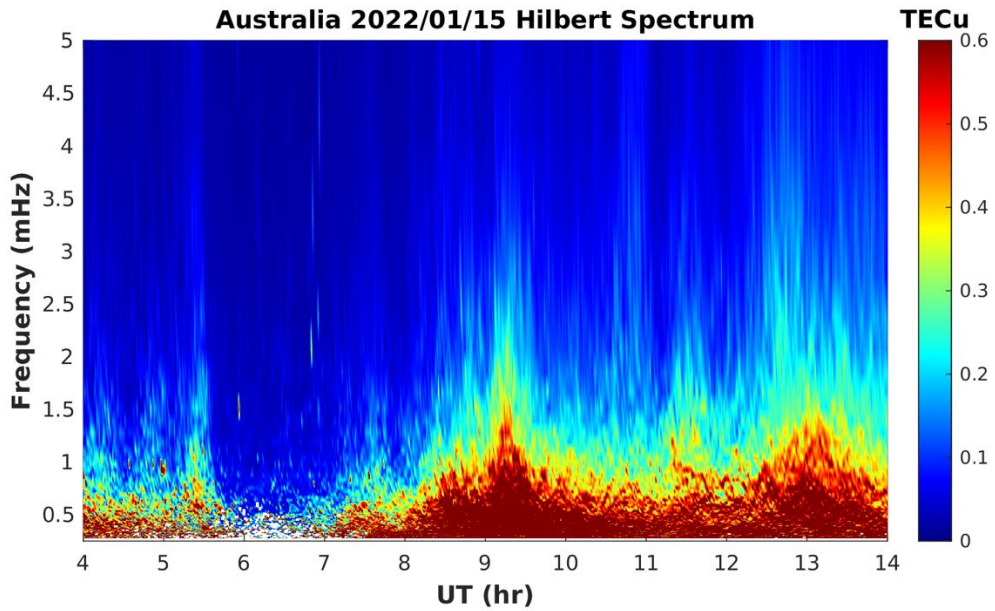
481 Whipple, F. J. W. (1930), The great siberian meteor and the waves, seismic and aerial, which it
482 produced, *Q. J. R. Meteorol. Soc.*, 56, 278-304.

483

484 Yeh, K. C., & Liu, C. H. (1974). Acoustic–gravity waves in the upper atmosphere. *Reviews of*
485 *Geophysics*, 12(2), 193–216.



486
 487 Figure 1. (a)-(d) Bandpass filtered TECs of 30-50 min periods showing the conjugate concentric TIDs after
 488 mapping Japan (Australia) TECs to Southern (Northern hemisphere), (e)-(h) with bandpass filter of 12-20
 489 min. The original TECs are plotted with “parula” colormap consisting of blue, green and yellow, while
 490 the conjugate TECs are plotted with “copper” colormap consisting of black and gold color.



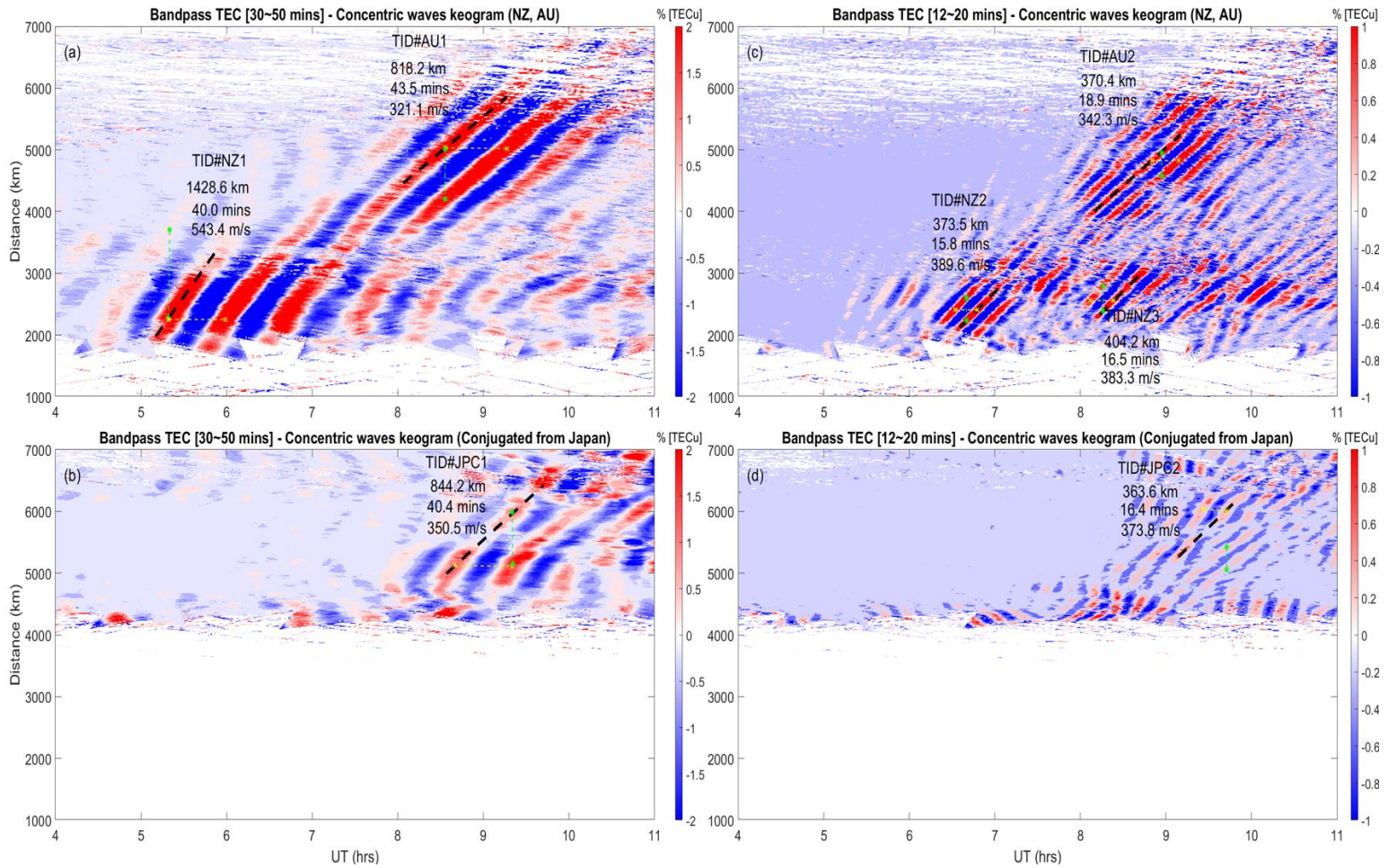
491

492 Figure 2. Hilbert Huang Transform of the TECs from Australia (top) and Japan (bottom) indicating the

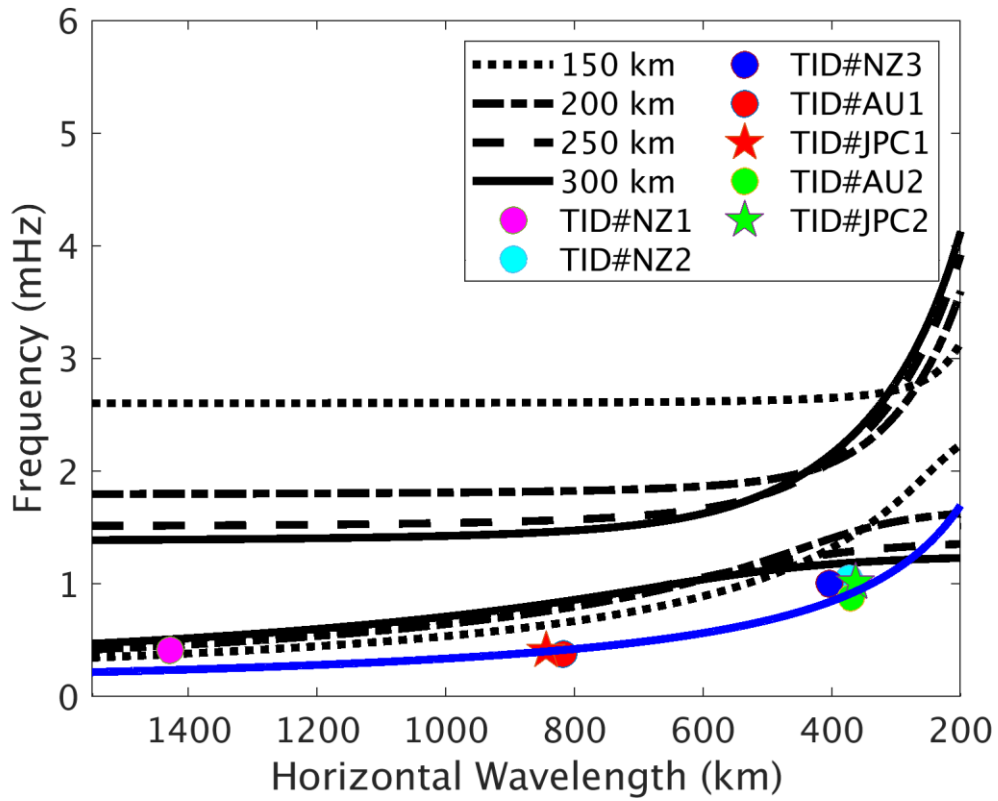
493 amplitude intensification after the eruption are manifest for frequency < 2 mHz (or 500s). The amplitude

494 intensifications around 0800-1000UT for both regions suggest the conjugate effect. The minimum

495 frequency in the vertical axes is set at 0.25 mHz (or 3600s).



496
 497 Figure 3. Keograms of the filtered TEC of 30-50 min (left) and 12-20 min (right) show the wave
 498 characteristics of CTIDs after 0400UT over New Zealand-Australia in (a) and (c), as the southern
 499 hemisphere conjugate locations of Japan are shown in (b) and (d). The distances are from the volcano to
 500 the sub-ionospheric point (SIP) locations over New Zealand and Australia areas, as observations over
 501 Japan have been mapped to the southern hemisphere.



502
 503 Figure 4. The theoretical dispersion curves of acoustic and gravity modes at 150 (dotted), 200 (dashed), 250
 504 (long-dashed) and 300 (solid) km altitudes are indicated in line plots. The colored dots/asterisk
 505 correspond to the observed TIDs shown in Figure 3. Blue solid line indicates the Lamb mode.

1 **Rapid Conjugate Appearance of the Giant Ionospheric Lamb Wave in the**
2 **Northern Hemisphere After Hunga-Tonga Volcano Eruptions.**

3

4 Jia-Ting Lin¹, Panthalingal K. Rajesh¹, Charles C. H. Lin¹, Min-Yang Chou^{2,3}, Jann-Yenq Liu^{4,5},
5 Jia Yue^{2,3}, Tung-Yuan Hsiao⁶, Ho-Fang Tsai¹, Hoi-Man Chao¹ and Mu-Min Kung¹

6

7 ¹Department of Earth Sciences, National Cheng Kung University, Tainan, Taiwan

8 ²NASA Goddard Space Flight Center, Community Coordinated Modeling Center, Greenbelt,
9 MD, USA

10 ³Physics Department, Catholic University of America, Washington, DC, USA

11 ⁴Center for Astronautical Physics and Engineering, National Central University, Taiwan

12 ⁵Department of Space Science and Engineer, National Central University, Taiwan

13 ⁶Nuclear Science and Technology Development Center, National Tsing Hua University, Hsinchu,
14 Taiwan

15 **Key points:**

- 16 1. Concentric traveling ionospheric disturbances (CTIDs) driven by volcano excited Lamb
17 wave are observed simultaneously in Australia and Japan.
- 18 2. Due to instantaneous magnetic field conjugate effect, the northern hemisphere CTIDs appear
19 3-hours prior to the arrival of surface Lamb wave
- 20 3. The CTIDs from conjugate hemispheres match with the theoretical dispersion relation of the
21 atmospheric Lamb mode.

22 **Abstract**

23 The explosive eruption of the Hunga-Tonga volcano in the southwest Pacific at 0415UT on
24 15 January 2022 triggered gigantic atmospheric disturbances with surface air pressure wave
25 propagating around the globe in Lamb mode. In space, concentric traveling ionosphere
26 disturbances (CTIDs) are also observed as a manifestation of air pressure acoustic waves in New
27 Zealand ~0500UT and Australia ~0630UT. As soon as the wave reached central Australia
28 ~0800UT, CTIDs appeared simultaneously in the northern hemispheres through magnetic field
29 line conjugate effect, which is much earlier than the arrival of the air pressure wave to Japan
30 after 1100UT. Combining observations over Australia and Japan between 0800-1000UT, CTIDs
31 with characteristics of phase velocities of 320-390 m/s are observed, matching with the
32 dispersion relation of Lamb mode. The arrival of atmospheric Lamb wave to Japan later created
33 in situ CTIDs showing the same Lamb mode characteristics as the earlier arriving CTIDs.

34 **Plain Language Summary**

35 The Hunga-Tonga Volcano eruption on 15 January 2022 has created the impulsive Lamb
36 wave propagation on the surface air pressure that has been observed globally. The Lamb wave,
37 typically moving at the sound speed of ~ 340 m/s, traveled 6 hours to reach Japan, but the Lamb
38 wave signature in the Earth's ionosphere, the ionized component of the atmosphere, arrived 3-
39 hours earlier than expected, thanks to the property of the ionospheric plasma being controlled by
40 the Earth's magnetic field. As soon as the surface Lamb wave reached Australia, the ionosphere
41 above showed concentric wave shape of the traveling ionospheric disturbances (TIDs) and the
42 effect was mapped to the northern hemisphere through the conductive magnetic field lines. This
43 is the first time such concentric waves from a volcanic eruption is observed simultaneously in
44 both the hemispheres. The much faster transmission of the ionosphere disturbances to the
45 northern hemisphere through the magnetic field lines is beyond expectations. Monitoring the
46 ionospheric disturbances could be a powerful early warning tool for the diagnosis of such
47 explosive events on the planet Earth.

48 **1. Introduction**

49 Although constrained along the magnetic field lines with gyro-motions, the plasma
50 distribution in the ionosphere, the ionized component of the Earth's atmosphere, could be
51 affected by perturbations in the neutral atmosphere through momentum transfer by ion-neutral
52 collisions (e.g. Heki and Ping, 2005), or through polarization electric field perpendicular to
53 magnetic field that drives $\delta E \times B$ electromagnetic drift across field lines (e.g. Chou et al., 2017a),
54 given that neutrals are abundant than ions at the ionospheric altitudes. Thus, neutral atmospheric
55 perturbations could be seen through the observations such as ionospheric total electron content
56 (TEC), and one of the signature forms of this coupling is the generation of traveling ionospheric
57 disturbances (TIDs). Such TIDs with shock acoustic characteristics occurred after rocket
58 launches accompanied by atmospheric perturbations (Lin et al., 2014; 2017a; Chou et al., 2018a).
59 Concentric TIDs (CTIDs), the feature of the concentric gravity wave effect to the ionosphere, are
60 observed associated with extreme weather systems in the lower atmosphere (e.g. Nishioka et al.,
61 2013; Chou et al., 2017b). There are events that created a broad spectrum of perturbations in
62 both acoustic and gravity wave modes, e.g., rocket launches that produce shock-acoustic waves
63 followed by concentric gravity waves (Lin et al., 2017b) or thermospheric ducted gravity waves
64 (Chou et al., 2018b). An extreme case is the 2011 Tohoku earthquake and tsunami which
65 triggered a diverse spectra of TIDs, including phase velocities of the high-speed Rayleigh wave
66 mode of ~ 3.5 km/s, acoustic mode of 1-1.2 km/s, gravity mode of ~ 300 -590 m/s and tsunami
67 mode of ~ 200 -250 m/s (e.g. Chen et al., 2011; Liu et al., 2011a; Rolland et al., 2011; Saito et al.,
68 2011; Tsugawa et al., 2011; Galvan et al., 2012; Azeem et al., 2017; Chou et al., 2020).

69 Additionally, explosive volcano events that release elevated plume to the atmosphere could
70 also produce TIDs (e.g. Heki, 2006), and most of the reported perturbations fall within the shock

71 and acoustic mode with frequencies of ~4-6 mHz. Shults et al. (2016) show that the eruption of
72 the Calbuco volcano on 22-23 April 2015 generated acoustic wave in the ionosphere with the
73 phase velocities of 900-1200 m/s. They also listed three other volcano events showing similar
74 phase velocity in the acoustic wave domain (Heki, 2006; Dautermann et al., 2009a, 2009b;
75 Nakashima et al., 2016). Nakashima et al. (2016) show TEC oscillations with frequencies of 3.7,
76 4.8 and 6.8 mHz, which are similar to the 4-6 mHz oscillations reported by Shults et al. (2016).
77 While these ionospheric perturbations in the acoustic mode reported in the above events were
78 limited within about 1000 km of the volcano source (Shults et al., 2016), one of the most
79 significant events that induced global atmosphere responses was the eruption of St. Helen on 18
80 May 1980. Liu et al. (1982) showed that the eruption of St. Helen created atmospheric pressure
81 disturbance waves and TIDs in the ionosphere worldwide. Their observations of TIDs could only
82 be explained by the propagation of the atmospheric Lamb wave modes with horizontal phase
83 velocity at the sound speed of ~310 m/s, with period ranging within 5-50 min.

84 Similar to the impacts reported during the St. Helen event, the recent Hunga Tonga - Hunga
85 Ha‘apai volcano eruption on 15 January 2022, sent out bouts of shock waves rippling through the
86 air, literally making the entire atmosphere to vibrate. The breathtaking images of the event
87 captured by Earth observing satellites show Lamb waves circulating the Earth, with worldwide
88 ground weather stations recording multiple passages of the air pressure waves (Duncombe, 2022).
89 The atmospheric disturbances from this violent eruption triggered a plethora of wave
90 perturbations, impacting the ocean surfaces and creating atmospheric oscillations, including
91 acoustic and gravity waves (e.g. Adam, 2022) that could potentially modulate the electron
92 content in the ionosphere. The TEC observations show CTID’s reaching several thousands of
93 kilometers away from the eruption source. Taking advantage of the dense Global Navigation

94 Satellite System (GNSS) receiver network over New Zealand, Australia, and Japan, we image
95 the Lamb wave perturbations in the ionosphere displaying CTIDs over Japan at least 3-hours
96 ahead of the expected arrival of the disturbances based on the estimates of the air pressure wave
97 propagation (according to the manuscript submitted at scientific online letters by Sekizawa and
98 Kohyama 2022; <https://doi.org/10.31223/X55K8V>, hereinafter referred to as Sekizawa and
99 Kohyama, 2022). This shows intriguing coupling from the magnetic conjugate regions in the
100 southern hemisphere. Chou et al. (2022) recently showed conjugate signatures of medium scale
101 traveling ionosphere disturbances (MSTID) produced by the tsunami propagation during the
102 2011 Tohoku earthquake. However, this is the first time such conjugate behavior of ionosphere
103 dynamo in coupling the polarization electric fields associated with concentric gravity waves
104 produced by the atmospheric perturbations from a volcanic eruption is observed. The wave
105 characteristics of the observed CTIDs and their conjugate appearances are discussed.

106

107 **2. GNSS TEC Observations**

108 The Hunga Tonga - Hunga Ha'apai islands (20.5S, 175.8 E) are rightly placed in the
109 proximity of the GNSS network maintained by Geological hazard information for New Zealand
110 and Geoscience Australia, offering the opportunity to examine the near field impact from the
111 volcanic eruption. Both the services combined adds up to about 600 GNSS receivers, receiving
112 signals from Global Positioning System (GPS) and GLObal Navigation Satellite System
113 (GLONASS) satellites. In addition, data from about 1300 stations of the GNSS network of the
114 Geospatial Information Authority of Japan and 140 stations of Central Weather Bureau of
115 Taiwan (Shin et al., 2011; 2013) are also used. Such dense networks, though limited to certain
116 regions, enables rapid examination of TEC variations with high spatial and temporal resolutions.

117 The information about the data sources is given in the Open Research section. The 30-second
118 sampled GNSS observations are used to derive vertical TEC at a sub-ionospheric altitude of 300
119 km, with a low elevation cut-off of 20° . The TEC variations are extracted by applying
120 Butterworth bandpass filters of 12-20 mins and 30-50 min to better present the small- and large-
121 scale atmospheric waves associated with the volcanic eruption before distributing to their
122 geolocations of the sub-ionospheric points (SIPs).

123 Figure 1 shows the time evolution of the filtered TEC maps for periods within 30-50 mins
124 and 12-20 mins at 0647, 0853, 0926 and 1120 UT. The filtered TECs projected to the conjugated
125 hemisphere using magnetic apex coordinates (Richmond, 1995; Emmert et al., 2010) are also
126 shown using different colormaps. Overplotted red dashed circles indicate the atmospheric
127 disturbances, mostly the Lamb wave, traveling at the speed of sound calculated using
128 temperature from NCEP reanalysis (Kalnay et al., 1998) and mean molecular mass from the
129 empirical NRLMSISE-00 model (Picone et al., 2002). According to Sekizawa and Kohyama
130 (2022), the arrival of the air pressure disturbances at Japan is ~ 1100 UT and the estimation
131 indicated by the dashed circles matches the arrival time. Liu et al. (1982) show from their model
132 calculation that the TIDs of acoustic-gravity waves associated with lamb modes are ~ 5 -50 mins
133 and we, therefore, focus on the TEC oscillations within these time periods. The bandpass
134 filtering is performed at 12-20 min (hereinafter referred as 12-20 wave) to illustrate the finer
135 structure of the CTIDs and at 30-50 min (hereinafter referred as 30-50 wave) to show the larger
136 scale CTIDs. The movie of the time evolutions of bandpass filtering of 12-20, 30-50 and 10-60
137 mins are provided in the supplementary material (Movie S1). In Figure 1 and movie S1, CTIDs
138 of both bands are seen clearly over New Zealand and Australia area after 0647UT and become
139 prominent and clearly conjugated, either mapping the Australia TECs to the northern hemisphere

140 or mapping the Japan TECs to the southern hemisphere after 0800UT. Thirty minutes ahead of
141 the arrival of the surface pressure wave in Japan, around 1030 UT, the propagation direction of
142 CTIDs in Japan started to turn from westward to north-westward, aligning perpendicular to the
143 wavefront of the surface waves. The 12-20 waves start to show direction change of the wavefront
144 ~1045UT, lagging ~15 minutes behind the 30-50 waves. The clear conjugated waves are still
145 seen in the southern hemisphere for the 12-20 wave after 1100UT upon the direct arrival of the
146 surface wave to Japan.

147 The spectral analysis of the GNSS TEC from both Australia and Japan has been performed
148 for oscillations of periods shorter than 1 h by using Hilbert-Huang transform (HHT, cf. Huang et
149 al., 1998; Liu et al., 2011b). Note that only TEC observations over the conjugate area (130-
150 140°E) are used to investigate the ionospheric conjugacy of CTIDs. Figure 2 shows the Hilbert
151 spectrum of TECs from both Australia and Japan. The amplitudes of both Hilbert spectra start to
152 intensify coherently ~0700UT and become prominent around 0800-1000UT, peaking at
153 ~0900UT for both regions for periods greater than 10 mins. Generally, the amplitude
154 intensifications occur after 0700UT for both spectra in the frequency range ~0.25-2 mHz or
155 period of 8-60 min, which is consistent with the 5-50 mins period suggested by Liu et al. (1982).

156 Figure 3 illustrate the keograms of the filtered TECs of New Zealand and Australia (Figs. 3a,
157 c) and Japan (Fig. 3b, d). As the filtered TECs over Japan are mapped to the southern hemisphere,
158 the distances to the volcano are counted from their southern hemisphere magnetic conjugate
159 locations. Figure 3a shows, for the 30-50 min period, that the first prominent packet of TIDs
160 appears clearly over New Zealand (distances < 3000 km) around 0500-0700UT. The second
161 prominent packet appears over Australia ~0700-1000UT. The 12-20 waves (Fig. 3c) lag behind

162 30-50 waves for at least 15 min or even longer. Clear conjugate effects for the two periods are
163 seen in the TIDs over Japan after 0730UT (Figs. 3c and 3d).

164 Except TID#NZ1, which shows phase velocity exceeding 500 m/s, most of the TIDs have
165 phase velocities of 320-390 m/s, and periods of ~40 mins for the 30-50 waves and 15-18 mins
166 for the 12-20 waves. These wave characteristics are further applied to estimate the dispersion
167 relation using Equation (1) (cf. Hines, 1960) expressed as follows. The equation is also utilized
168 to calculate the dispersion curves of acoustic and gravity modes.

$$169 \quad m^2 = \left(1 - \frac{\omega_a^2}{\omega^2}\right) \frac{\omega^2}{c_0^2} - k^2 \left(1 - \frac{\omega_b^2}{\omega^2}\right) \quad (1)$$

170 where m is the complex vertical wave number, $\omega_a = \sqrt{\frac{\gamma g}{4H} + \frac{g}{T} \frac{dT}{dz}}$ is acoustic cutoff frequency,

171 $\omega_b = \sqrt{\frac{(\gamma-1)g}{\gamma H} + \frac{g}{T} \frac{dT}{dz}}$ is buoyancy frequency, $\omega = k(c_h - u)$ is intrinsic frequency, u is the

172 neutral wind speed in the direction of wave propagation, c_h is the horizontal phase velocity, H is

173 the scale height, γ is the ratio of specific heats, g is the gravitational acceleration, and T is neutral

174 temperature. These parameters are adopted from empirical neutral atmospheric parameters from

175 the Horizontal Wind Model 2014 (Drob et al., 2015) and NRLMSISE-00. The acoustic-gravity

176 wave is evanescent or freely propagating while $m^2 < 0$ or $m^2 > 0$. We identify the characteristic of

177 these TIDs by calculating the dispersion curves for Figure 4 ($m^2 = 0$) using equation (1) (cf. Yeh

178 and Liu, 1974; Matsumura et al., 2012). The black solid, dashed, dashed-dot and dotted lines

179 indicate the dispersion curves of gravity mode and acoustic mode at 300, 250, 200 and 150 km

180 altitude, respectively. The colored dots indicate the calculated intrinsic frequencies of observed

181 TIDs indicated in Figure 3. The Lamb wave mode with constant phase velocity of sound is added

182 with the blue solid line in Figure 4. It is seen that the color dots of TIDs are aligned along the
183 blue solid line indicating the Lamb wave signature of CTIDs observed in this study.

184 Since atmospheric Lamb wave has non-dispersive characteristics as acoustic waves (Francis,
185 1973), it is expected to see similar wave characteristics of CTIDs over Japan after the actual
186 arrival of the Lamb wave to Japan ~1100UT. Figure S2 shows the 30-50 and 12-20 waves over
187 Japan ~1000-1400UT. It indicates that the 30-50 waves again lead the 12-20 wave, and these
188 waves generally fit along the curve of Lamb mode, except the early appearance of 12-20 waves
189 (TID#JP6, JP7 and JP8).

190

191 **3. Discussions and Conclusion**

192 We present the first clear images of CTIDs propagating with the Lamb mode driven by the
193 volcano excited Lamb wave for the first time (Fig. 1). Taking advantage of the magnetic
194 conjugate effect by combining observations from Australia and Japan, a comprehensive picture
195 of concentric waves could be drawn, and their wave characteristics are all consistent with the
196 dispersion relation of Lamb mode as shown in Figs. 3 and 4. Another important discovery is that
197 the CTIDs could be seen conjugately even during daytime (Dusk), which was not previously
198 reported in the literature. This new finding suggests that the Lamb wave excited by the explosive
199 Hunga Tonga - Hunga Ha'apai volcano could affect the global ionosphere much sooner than
200 expected as the driven CTIDs are capable of being transmitted to the magnetically conjugate
201 hemispheres.

202 During the geomagnetically quiescent period, the magnetic conjugate effect of the
203 ionosphere is well known and there are studies on the conjugate effect of plasma instabilities
204 during nighttime, such as equatorial plasma bubble (EPB) and MSTID (e.g. Otsuka et al., 2004;

205 Fukushima et al., 2015; Valladares and R. Sheehan, 2016). During daytime the conjugate effect
206 is believed to be rare because the efficiency of electric field mapping is proportional to the ratio
207 of field line integration of the Pedersen conductivities in F- and E-regions as $\frac{\Sigma_p^F}{\Sigma_p^F + \Sigma_p^E}$. The much
208 higher E-region conductivity during daytime then prevents the electric field mapping in the F-
209 region. However, some exceptions were observed by Jonah et al. (2017) and they adopted the
210 explanation given by Abdu et al. (2015) that during the late afternoon approaching the sunset
211 hours, the ratio of F- and E-region conductivities could be close to 0.8 or greater making electric
212 field mapping likely to happen. Our observation of the Lamb wave driven CTIDs in Japan
213 appeared after 0730UT or 1630LT, close to the time-period when the mapping is likely favored.

214 The 2011 Great Tohoku earthquake and tsunami also triggered conjugate effect of the
215 tsunami driven gravity waves, but they were mainly during nighttime. Huba et al. (2015)
216 simulated the conjugate ionospheric effects associated with the tsunami-driven gravity waves
217 using self-consistent electrodynamics and suggested that the perpendicular neutral wind
218 perturbation could induce polarization electric fields mapping along the geomagnetic field line to
219 the conjugate southern hemisphere of Hawaii. Their simulations were compared with the sparse
220 GPS-derived TEC when the tsunami passed by Hawaii during nighttime. Chou et al. (2022)
221 discovered that the reflected tsunami was able to drive gravity waves over Japan and triggered
222 prominent MSTID occurring in March, a season of rare MSTID occurrence, and further mapped
223 to the conjugate southern hemisphere over Australia. However, the initial main TIDs driven by
224 the earthquake and tsunami did not produce any conjugate effect, and the coupled gravity wave-
225 Perkins instability may contribute to the interhemispheric conjugate process due to the specific
226 wavefront alignment of the MSTIDs. This study, therefore, provides direct observational

227 evidence to support that wind-dynamo coupling (e.g., Huba et al., 2015) alone is sufficient to
228 induce the conjugate effect.

229 Surface air pressure wave traveling with Lamb mode occurred during previous explosion
230 events, e.g. Kratatoa volcano eruption in 1883 (Pekeries, 1939), Tunguska event in Siberia 1908
231 (Whippe, 1930) and St. Helen eruption in 1980 (Liu et al., 1980). According to Francis (1973),
232 the lower atmosphere Lamb wave could propagate long distances with little dissipation and its
233 attenuation distance, defined by attenuation by a factor of $1/e$, is of the order of Earth's
234 circumference or greater. The non-dispersive and weak attenuation properties of the air pressure
235 wave (Duncombe, 2022) again suggest that it is the Lamb wave traveling globally, excited by the
236 volcano eruption, being studied here. The ionosphere disturbances also show weak attenuation
237 feature. The amplitudes of the CTIDs (percentage of TEC perturbations) over New Zealand-
238 Australia around 0500-1000UT (Figs. 3a and 3b) and Japan, more than 8000 km away from the
239 volcano, around 1000-1300UT, are comparable (Fig S2), indicating the weak attenuation nature
240 of the Lamb wave. Although the Lamb wave generally travels in the troposphere and
241 stratosphere below about 30 km altitude and its energy decreases with altitudes, the exponential
242 decrease of neutral density with increasing altitude actually increases its amplitude. Additionally,
243 Nishida et al. (2014) show that Lamb wave could theoretically exist at thermosphere altitudes.
244 Our observations of CTIDs agree with the dispersion relation of Lamb mode and the weak
245 attenuation suggests that the CTIDs driven by the Hunga-Tonga volcano have Lamb wave
246 characteristics.

247 It is worthwhile to note that (according to Fig. 1 and Movie S1), prior to the arrival of the air
248 pressure Lamb wave to Australia, there are already signatures of TIDs. By comparing with the
249 intense tsunami effect of the 2011 Tohoku earthquake, there were leading TIDs ahead of the

250 tsunami arrival (e.g. Makela et al., 2011). Inchin et al. (2020) suggest that the tsunami-induced
251 gravity wave spectrum has phase variations from long-period phases at the head of the packet to
252 short-period phases at its tail. A similar process might occur in this event, where, instead of the
253 tsunami exciting the gravity waves the surface Lamb wave might excite a broad spectrum of
254 gravity waves. Gravity waves with longer period waves travel faster than short period waves
255 (Figs. 1, 3, S2). Gravity waves with the period locked to the dominant period of Lamb mode will
256 eventually travel at the same speed of surface pressure wave after reaching the ionosphere and
257 the surface pressure Lamb wave plays the role of continuously triggering gravity wave as a
258 moving source. This process is also similar to the seismic Rayleigh wave that continuously
259 excites seismo-TIDs with the same periods and speeds (e.g., Liu et al., 2011a).

260 Rakoto et al. (2017) developed the ocean-atmosphere coupled model for tsunami effects
261 with analyses of acoustic, gravity, tsunami and Lamb modes. They find that the tsunami mode
262 does not transfer energy to the Lamb mode through resonance as their frequency branches are
263 not crossing each other. On the other hand, the tsunami mode could excite gravity waves due to
264 the crossing frequency branches of the tsunami and gravity modes. Similarly, for the volcano
265 effect discussed here, the Lamb mode frequency crosses through the frequencies of gravity
266 modes (Figs. 4 and S3) and it is likely that the Lamb wave could thereby induce a packet of
267 gravity waves. The lagged 12-20 waves in Fig. 1 and the keograms of Figs. 3 and S2 showing the
268 smaller scale waves appearing at later times suggest that such a process might be operational.

269 It is noted that there was a minor magnetic storm during the volcano eruption, with the
270 disturbance storm index (Dst) dropping to about -94 nT at ~2300 UT on 14 January 2022.
271 Magnetic storms are known to generate large-scale TIDs (LSTIDs) that propagate equatorward
272 (e.g., Richmond, 1978), and could give rise to TEC perturbations (Cherniak and Zakharenkova,

273 2018). However, the storm influence could be ruled out here to have any role in producing the
274 TEC observed fluctuations after the eruption. Though interplanetary magnetic field (IMF Bz)
275 turned southward after 1800 UT on this day, gradually reaching about -18 nT by 2230 UT, the
276 solar wind velocity was only 350-380 km/s during this period and the proton density did not
277 increase much, suggesting only minor storm impact. The auroral electrojet (AE) index, which
278 briefly reached over 1000 during 2100-2200 UT, and again spiked for a few minutes before 2300
279 UT on 01/14 when IMF Bz was southward, returned to values below 500 before 0000 UT on
280 01/15 and subsequently remained subdued, further indicating lack of any significant high latitude
281 activity. The IMF Bz also turned northward by 2330 UT on 01/14, and later revealed fluctuations
282 typical of CIR events. The Dst index further shows that by the time the eruption occurred, the
283 storm was well into the recovery phase. Moreover, LSTIDs usually propagate equatorward from
284 high latitudes, whereas the observed perturbations show CTIDs expanding poleward as the Lamb
285 waves circulated the Earth.

286 In conclusion, we present the first comprehensive picture of the concentric traveling
287 ionospheric disturbances in conjugate hemispheres coherently showing the Lamb wave
288 characteristic driven by the powerful eruption of Hunga Tonga - Hunga Ha'apai. The varying
289 phase velocities of the ionospheric disturbances with different wave periods suggest that the
290 Lamb waves excite a broad spectra of gravity waves, further indicating resonant wave-coupling
291 of co-existing Lamb and gravity modes. The conductive geomagnetic field lines enable the rapid
292 transmission of disturbance waves to the northern hemisphere on Alfvénic timescales (~300
293 km/s), leading to rapid electrified ionospheric disturbances faster than the direct Lamb waves
294 over Japan, which is beyond expectations. The GNSS networks therefore could be a powerful

295 tool for early warning system for the diagnosis of such explosive events on the planet Earth, and
296 advance our understanding of how natural hazards drive space weather.

297

298

299 **Acknowledgements**

300 This work is partly supported by the Ministry of Science and Technology under MOST 110-
301 2111-M-006-004 and MOST 110-2119-M-006-001. MYC was supported by NASA grant
302 80NSSC20K0628. CHL wishes to thank Chao-Han Liu for useful discussions. The authors
303 acknowledge the Geological hazard information for New Zealand, the Geoscience Australia, the
304 Geospatial Information Authority of Japan, the Central Weather Bureau, Taiwan for managing
305 the GNSS observations, and the Geomagnetic Data Service of Kyoto University and NOAA
306 Space Weather Prediction Center for geomagnetic and solar wind parameters.

307

308 **Open Research**

309 The GNSS RINEX data are available from the Geological hazard information for New Zealand
310 (GeoNet, <https://www.geonet.org.nz/data/types/geodetic>), the Geoscience Australia GNSS data
311 archive (<https://www.ga.gov.au/scientific-topics/positioning-navigation/geodesy/gnss-networks>),
312 the Geospatial Information Authority of Japan (GEONET,
313 https://www.gsi.go.jp/ENGLISH/geonet_english.html) and the Geophysical Database
314 Management System of Central Weather Bureau, Taiwan (<https://gdms.cwb.gov.tw/index.php>).
315 Dst and AE indices are available at the Geomagnetic Data Service of Kyoto University
316 (<http://wdc.kugi.kyoto-u.ac.jp/wdc/Sec3.html>) and the solar wind parameters could be accessed
317 from NOAA Space Weather Prediction Center (<https://www.swpc.noaa.gov/products/real-time->

318 solar-wind). The processed TEC data is available at
319 <https://doi.org/10.6084/m9.figshare.19115624>.

320

321 **Reference**

322 Abdu, M. A., J. R. de Souza, E. A. Kherani, I. S. Batista, J. W. MacDougall, and J. H. A. Sobral
323 (2015), Wave structure and polarization electric field development in the bottomside F
324 layer leading to postsunset equatorial spread F, *J. Geophys. Res. Space Physics*, 120,
325 6930–6940, doi:10.1002/2015JA021235.

326 Adam, D. (2022), Tonga volcano eruption created puzzling ripples in Earth’s atmosphere,
327 *Nature* **601**, 497.

328 Azeem, I., Vadas, S. L., Crowley, G., and Makela, J. J. (2017), Traveling ionospheric
329 disturbances over the United States induced by gravity waves from the 2011 Tohoku
330 tsunami and comparison with gravity wave dissipative theory, *J. Geophys. Res. Space*
331 *Physics*, 122, 3430– 3447, doi:10.1002/2016JA023659.

332 Chen, C. H., A. Saito, C. H. Lin, J. Y. Liu, H. F. Tsai, T. Tsugawa, Y. Otsuka, M. Nishioka and
333 M. Matsumura (2011), Long-distance propagation of ionospheric disturbance generated by
334 the 2011 Tohoku earthquake, *Earth Planets and Space*, 63, 7, 881-884,
335 doi:10.5047/eps.2011.06.026

336 Cherniak, I., and Zakharenkova, I. (2018). Large-scale traveling ionospheric disturbances origin
337 and propagation: Case study of the December 2015 geomagnetic storm. *Space Weather*, 16,
338 1377– 1395. <https://doi-org.cuucar.idm.oclc.org/10.1029/2018SW001869>

339 Chou, M. Y., C. H. Lin, J. Yue, L. C. Chang, H. F. Tsai and C. H. Chen (2017a), Medium-scale
340 traveling ionospheric disturbances triggered by Super Typhoon Nepartak (2016), *Geophys.*
341 *Res. Lett.*, 44, 7569–7577, doi:10.1002/2017GL073961

342 Chou, M. Y., C. H. Lin, J. Yue, H. F. Tsai, Y. Y. Sun, J. Y. Liu and C. H. Chen (2017b),
343 Concentric traveling ionosphere disturbances triggered by Super Typhoon Meranti (2016),
344 *Geophys. Res. Lett.*, 44, doi:10.1002/2016GL072205.

345 Chou, M. Y., M. H. Shen, C. H. Lin, J. Yue, C. H. Chen, J. Y. Liu and J. T. Lin (2018a),
346 Gigantic circular shock acoustic waves in the ionosphere triggered by the launch of
347 FORMOSAT-5 satellite, *Space Weather*, 16, 172-184, doi:10.1002/2017SW001738.

348 Chou, M.-Y., Lin, C. H., Shen, M.-H., Yue, J., Huba, J. D., & Chen, C.-H. (2018b), Ionospheric
349 disturbances triggered by SpaceX Falcon Heavy, *Geophysical Research*
350 *Letters*, 45, doi:10.1029/2018GL078088.

351 Chou, M.-Y., Cherniak, I., Lin, C. C. H., & Pedatella, N. M. (2020). The persistent ionospheric
352 responses over Japan after the impact of the 2011 Tohoku earthquake. *Space Weather*, 18,
353 e2019SW002302. <https://doi.org/10.1029/2019SW002302>

354 Chou, M.-Y., Yue, J., Lin, C. C. H., Rajesh, P. K., & Pedatella, N. M. (2022). Conjugate effect
355 of the 2011 Tohoku reflected tsunami-driven gravity waves in the ionosphere. *Geophysical*
356 *Research Letters*, 49, e2021GL097170, doi:10.1029/2021GL097170.

357 Dautermann, T., Calais, E., Lognonné, P., Mattioli, G.S., 2009a. Lithosphere– atmosphere–
358 ionosphere coupling after the 2003 explosive eruption of the Soufriere Hills Volcano,
359 Montserrat. *Geophys. J. Int.* 179 (3), 1537–1546.

360 Dautermann, T., Calais, E., Mattioli, G.S., 2009b. Global positioning system detection and
361 energy estimation of the ionospheric wave caused by the 13 July 2003 explosion of the

362 Soufrière Hills Volcano, Montserrat. *J. Geophys. Res.* 114 (B2), B02202.
363 doi:10.1029/2008JB005722.

364 Drob, D. P., Emmert, J. T., Meriwether, J. W., Makela, J. J., Doornbos, E., Conde, M., et al.
365 (2015). An update to the horizontal wind model (HWM):The quiet time thermosphere. *Earth*
366 *Space Science*, 2(7), 301–319. <https://doi.org/10.1002/2014EA000089>

367 Duncombe, J. (2022), The surprising reach of Tonga’s giant atmospheric waves, *Eos*, 103,
368 <https://doi.org/10.1029/2022EO220050>.

369 Emmert, J. T., A. D. Richmond, and D. P. Drob (2010), A computationally compact
370 representation of Magnetic-Apex and Quasi-Dipole coordinates with smooth base vectors,
371 *J. Geophys. Res.*, 115(A8), A08322, doi:10.1029/2010JA015326.

372 Francis, S. H. (1973), Acoustic-gravity modes and large-scale traveling ionospheric disturbances
373 of a realistic, dissipative atmosphere, *J. Geophys. Res.*, 78(13), 2278– 2301,
374 doi:[10.1029/JA078i013p02278](https://doi.org/10.1029/JA078i013p02278).

375 Fukushima, D., Shiokawa, K., Otsuka, Y., Nishioka, M., Kubota, M., Tsugawa, T., Nagatsuma,
376 T., Komonjinda, S., and Yatini, C. Y. (2015), Geomagnetically conjugate observation of
377 plasma bubbles and thermospheric neutral winds at low latitudes. *J. Geophys. Res. Space*
378 *Physics*, 120, 2222– 2231. doi: [10.1002/2014JA020398](https://doi.org/10.1002/2014JA020398).

379 Galvan, D. A., Komjathy, A., Hickey, M. P., Stephens, P., Snively, J., Tony Song, Y., Butala, M.
380 D., and Mannucci, A. J. (2012), Ionospheric signatures of Tohoku-Okii tsunami of March
381 11, 2011: Model comparisons near the epicenter, *Radio Sci.*, 47, RS4003,
382 doi:[10.1029/2012RS005023](https://doi.org/10.1029/2012RS005023).

383 Heki, K., and J. Ping (2005), Directivity and apparent velocity of the coseismic ionospheric
384 disturbances observed with a dense GPS array, *Earth Planet. Sci. Lett.*, 236, 845–855,
385 doi:10.1016/j.epsl.2005.06.010.

386 Heki, K. (2006), Explosion energy of the 2004 eruption of the Asama Volcano, central Japan,
387 inferred from ionospheric disturbances, *Geophys. Res. Lett.*, 33, L14303,
388 doi:10.1029/2006GL026249.

389 Hines, C. O. (1960), Internal atmospheric gravity waves at ionospheric heights, *Can. J. Phys.*, 38,
390 1441.

391 Huang, N. E., et al. (1998), The empirical mode decomposition and the Hilbert spectrum for
392 nonlinear and nonstationary time series analysis, *Proc. R. Soc. London, Ser. A*, 454, 903–
393 995, doi:10.1098/rspa.1998.0193.

394 Huba, J. D., G. Joyce, and J. Krall (2008), Three-dimensional equatorial spread F modeling,
395 *Geophys. Res. Lett.*, 35, L10102, doi:10.1029/2008GL033509.

396 Huba, J. D., D. P. Drob, T.-W. Wu, and J. J. Makela (2015), Modeling the ionospheric impact of
397 tsunami-driven gravity waves with SAMI3: Conjugate effects, *Geophys. Res. Lett.*, 42,
398 5719–5726, doi:10.1002/2015GL064871.

399 Inchin, P. A., Heale, C. J., Snively, J. B., & Zettergren, M. D. (2020). The dynamics of nonlinear
400 atmospheric acoustic-gravity waves generated by tsunamis over realistic bathymetry.
401 *Journal of Geophysical Research: Space Physics*, 125, e2020JA028309.
402 <https://doi.org/10.1029/2020JA028309>

403 Jonah, O. F., E. A. Kherani, and E. R. De Paula (2017), Investigations of conjugate MSTIDS
404 over the Brazilian sector during daytime, *J. Geophys. Res. Space Physics*, 122, 9576–9587,
405 doi:10.1002/2017JA024365.

406 Kalnay, E., Kanamitsu, M., Kistler, R., Collins, W., Deaven, D., Gandin, L., Iredell, M., Saha,
407 S., White, G., Woollen, J., Zhu, Y., Chelliah, M., Ebisuzaki, W., Higgins, W., Janowiak, J.,
408 Mo, K. C., Ropelewski, C., Wang, J., Leetmaa, A., Reynolds, R., Jenne, R., & Joseph, D.
409 (1996). The NCEP/NCAR 40-Year Reanalysis Project, *Bulletin of the American*
410 *Meteorological Society*, 77(3), 437-472. Retrieved Feb 6, 2022, from
411 [https://journals.ametsoc.org/view/journals/bams/77/3/1520-](https://journals.ametsoc.org/view/journals/bams/77/3/1520-0477_1996_077_0437_tnyrp_2_0_co_2.xml)
412 [0477_1996_077_0437_tnyrp_2_0_co_2.xml](https://journals.ametsoc.org/view/journals/bams/77/3/1520-0477_1996_077_0437_tnyrp_2_0_co_2.xml)

413 Lin, C. H., Lin, J. T. Lin, C. H. Chen, M. Matsumura, J. Y. Liu, Y. Y. Sun, W. H. Chen, Y.
414 Kakinami, H. Liu, and R. J. Rau (2014), Ionospheric Shock Waves Triggered by Rockets,
415 *Ann. Geophys.*, 32, 9, 1145–1152, doi:10.5194/angeo-32-1145-2014

416 Lin, C. H. , C. H. Chen, M. Matsumura, J.-T. Lin and Y. Kakinami (2017a), Observation and
417 simulation of the ionospheric disturbance waves triggered by rocket exhausts, *J. Geophys.*
418 *Res. Space Physics*, 122, doi:10.1002/2017JA023951.

419 Lin, C. H., M. H. Shen, M. Y. Chou, C. H. Chen, J. Yue, P. C. Chen, and M. Matsumura (2017b),
420 Concentric traveling ionospheric disturbances triggered by the launch of a SpaceX Falcon
421 9 rocket, *Geophys. Res. Lett.*, 44, 7578–7586, doi:10.1002/2017GL074192.

422 Liu, C. H., et al. (1982), Global dynamic responses of the atmosphere to the eruption of Mount
423 St. Helens on May 18, 1980, *J. Geophys. Res.*, 87(A8), 6281– 6290,
424 doi:[10.1029/JA087iA08p06281](https://doi.org/10.1029/JA087iA08p06281).

425 Liu, J.-Y., C.-H. Chen, C.-H. Lin, H.-F. Tsai, C.-H. Chen, and M. Kamogawa (2011a),
426 Ionospheric disturbances triggered by the 11 March 2011 M9.0 Tohoku earthquake, *J.*
427 *Geophys. Res.*, 116, A06319, doi:10.1029/2011JA016761.

428 Liu, J. Y., Y. Y. Sun, Y. Kakinami, C. H. Chen, C. H. Lin, and H. F. Tsai (2011b), Bow and
429 stern waves triggered by the Moon's shadow boat, *Geophys. Res. Lett.*, 38, L17109,
430 doi:10.1029/2011GL048805.

431 Makela, J. J., et al. (2011), Imaging and modeling the ionospheric airglow response over Hawaii
432 to the tsunami generated by the Tohoku earthquake of 11 March 2011, *Geophys. Res. Lett.*,
433 38, L00G02, doi:10.1029/2011GL047860.

434 Matsumura, M., H. Shinagawa, and T. Iyemori (2012), Horizontal extension of acoustic
435 resonance between the ground and the lower thermosphere, *J. Atmos. Sol. Terr. Phys.*, 75-76,
436 127–132.

437 Nakashima, Y., K. Heki, A. Takeo, M. N. Cahyadi, A. Aditiya, and K. Yoshizawa (2016),
438 Atmospheric resonant oscillations by the 2014 eruption of the Kelud volcano, Indonesia,
439 observed with the ionospheric total electron contents and seismic signals, *Earth Planet. Sci.*
440 *Lett.*, 434, 112–116, doi:10.1016/j.epsl.2015.11.029.

441 Nishida, K., N. Kobayashi and Y. Fukao (2014), Background Lamb waves in the Earth's
442 atmosphere, *Geophys. J. Int.*, 196, 312–316, doi: 10.1093/gji/ggt413

443 Otsuka, Y., K. Shiokawa, T. Ogawa, and P. Wilkinson (2004), Geomagnetic conjugate
444 observations of medium-scale traveling ionospheric disturbances at midlatitude using all-
445 sky airglow imagers, *Geophys. Res. Lett.*, 31, L15803, doi:10.1029/2004GL020262.

446 Pekeris, C. L. (1939), The propagation of a pulse in the atmosphere, *Proc. R. Soc. London Ser. A*,
447 A171, 434-449.

448 Picone, J. M., A. E. Hedin, D. P. Drob, and A. C. Aikin (2002), NRLMSISE-00 empirical model
449 of the atmosphere: Statistical comparisons and scientific issues, *J. Geophys. Res.*, 107
450 (A12), 1468, doi:10.1029/2002JA009430.

451 Rakoto, V., P. Lognonné, L. Rolland (2017), Tsunami modeling with solid Earth–ocean–
452 atmosphere coupled normal modes, *Geophysical Journal International*, Oxford University
453 Press (OUP), 2017, 211 (2), pp.1119 - 1138. 10.1093/gji/ggx322 . hal-01737686

454 Richmond, A. D. (1978), Gravity wave generation, propagation, and dissipation in the
455 thermosphere, *J. Geophys. Res.*, 83(A9), 4131– 4145, doi:10.1029/JA083iA09p04131.

456 Richmond, A. D., Ionospheric electrodynamics using Magnetic Apex Coordinates, *J. Geomagn.*
457 *Geoelectr.*, 47, 191–212, 1995.

458 Rolland, L.M., Lognonné, P., Astafyeva, E. *et al.* The resonant response of the ionosphere
459 imaged after the 2011 off the Pacific coast of Tohoku Earthquake. *Earth Planet Sp* **63**, 62
460 (2011). <https://doi.org/10.5047/eps.2011.06.020>

461 Saito, A., Tsugawa, T., Otsuka, Y., Nishioka, M., Iyemori, T., Matsumura, M., Saito, S., Chen,
462 C.H., Goi, Y., Choosakul, N., 2011. Acoustic resonance and plasma de- pletion detected by
463 GPS total electron content observation after the 2011 off the Pacific coast of Tohoku
464 Earthquake. *Earth Planets Space* 63 (7), 863–867, doi:10.5047/eps.2011.06.034.

465 Shin, T. C., K. W. Kuo, P. L. Leu, C. H. Tsai, and J. S. Jiang, 2011: Continuous CWB GPS array
466 in Taiwan and applications to monitoring seismic activity. *Terr. Atmos. Ocean. Sci.*, 22,
467 521-533, doi: 10.3319/TAO.2011.05.18.01(T)

468 Shin, T. C., C. H. Chang, H. C. Pu*, H. W. Lin, and P. L. Leu, 2013: The Geophysical Database
469 Management System in Taiwan. *Terr. Atmos. Ocean. Sci.*, 24, 11-18, doi:
470 10.3319/TAO.2012.09.20.01(T)

471 Shults, K., E. Astafyeva, and S. Adourian (2016), Ionospheric detection and localization of
472 volcano eruptions on the example of the April 2015 Calbuco events, *J. Geophys. Res.*
473 *Space Physics*, 121, 10,303–10,315, doi:10.1002/2016JA023382.)

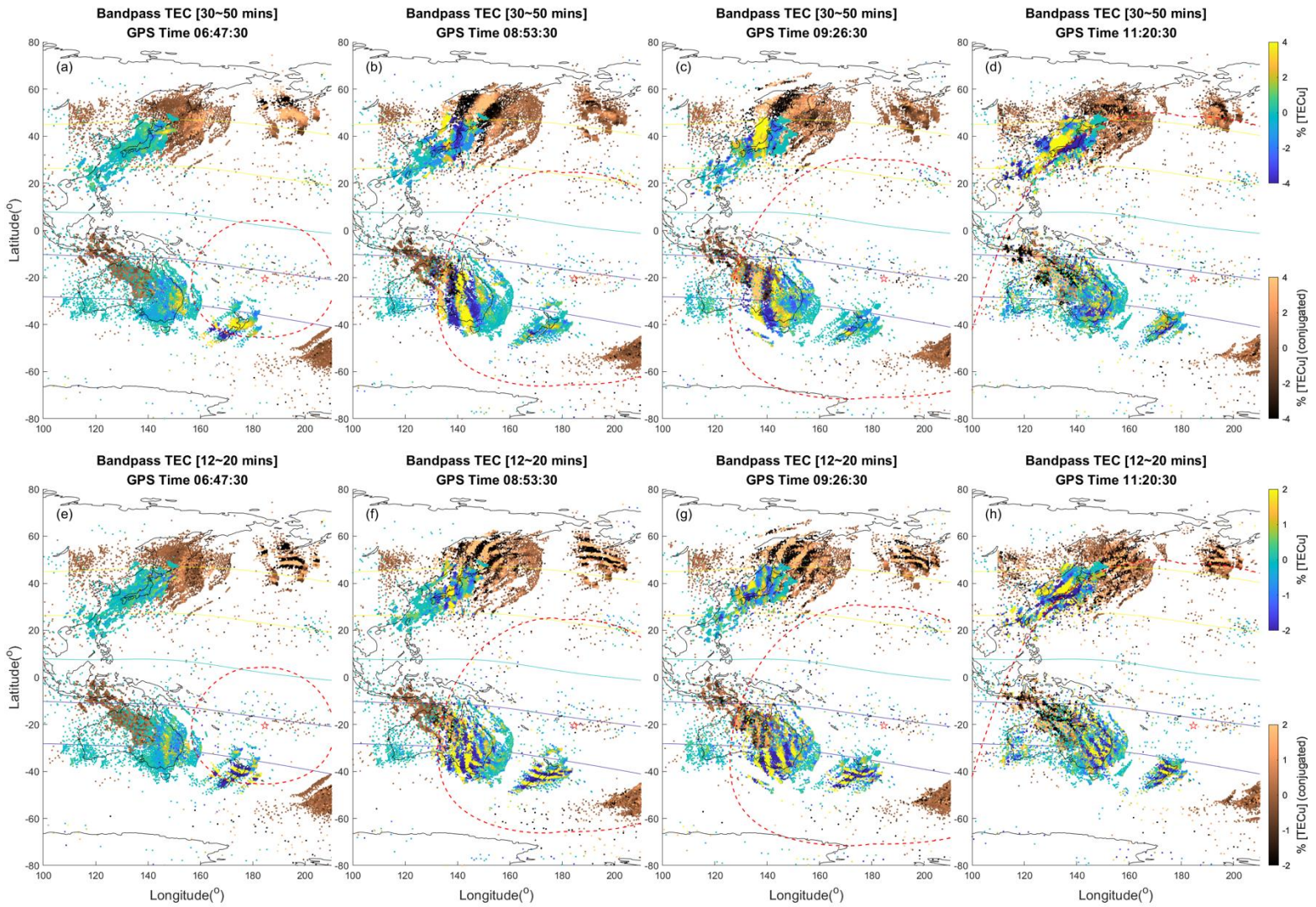
474 Tsugawa, T., A. Saito, Y. Otsuka, M. Nishioka, T. Maruyama, H. Kato, T. Nagatsuma, and K. T.
475 Murata, Ionospheric disturbances detected by GPS total electron content observation after
476 the 2011 off the Pacific coast of Tohoku Earthquake, *Earth Planets Space*, **63**, this issue,
477 875–879, 2011.

478 Valladares, C. E., and R. Sheehan (2016), Observations of conjugate MSTIDs using networks of
479 GPS receivers in the American sector, *Radio Sci.*, 51, 1470–1488,
480 doi:10.1002/2016RS005967.

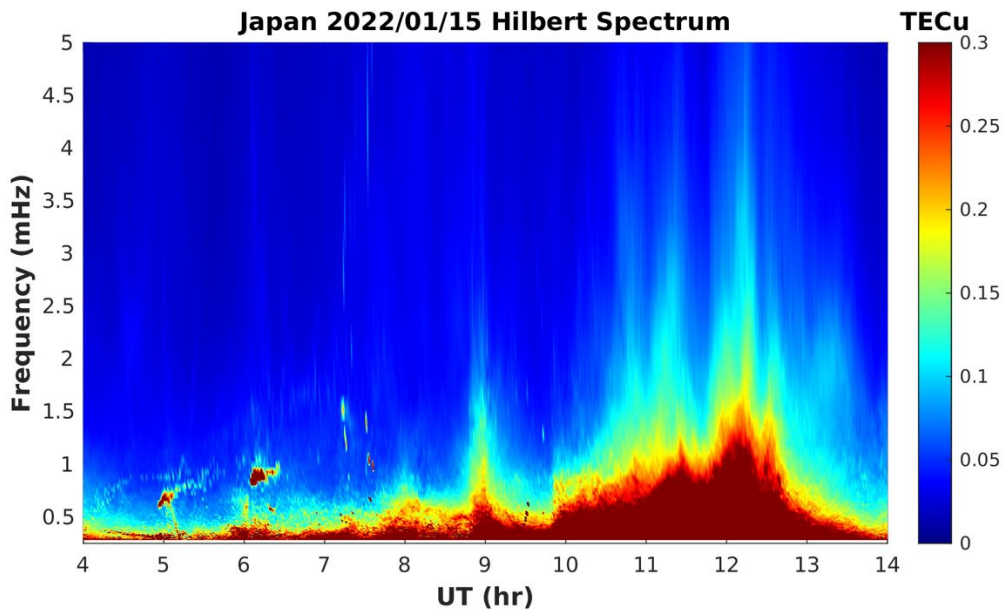
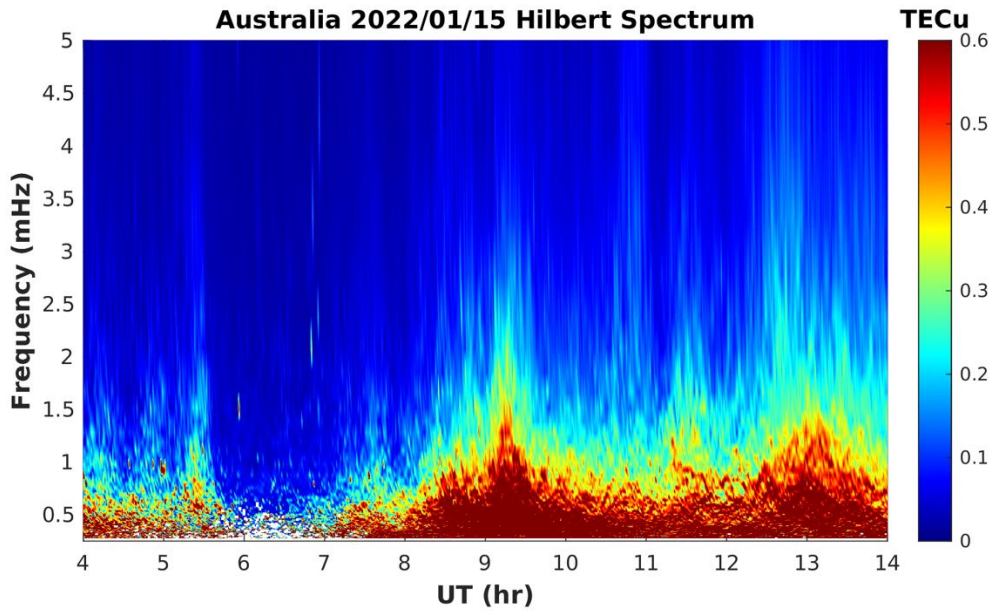
481 Whipple, F. J. W. (1930), The great siberian meteor and the waves, seismic and aerial, which it
482 produced, *Q. J. R. Meteorol. Soc.*, 56, 278-304.

483

484 Yeh, K. C., & Liu, C. H. (1974). Acoustic–gravity waves in the upper atmosphere. *Reviews of*
485 *Geophysics*, 12(2), 193–216.

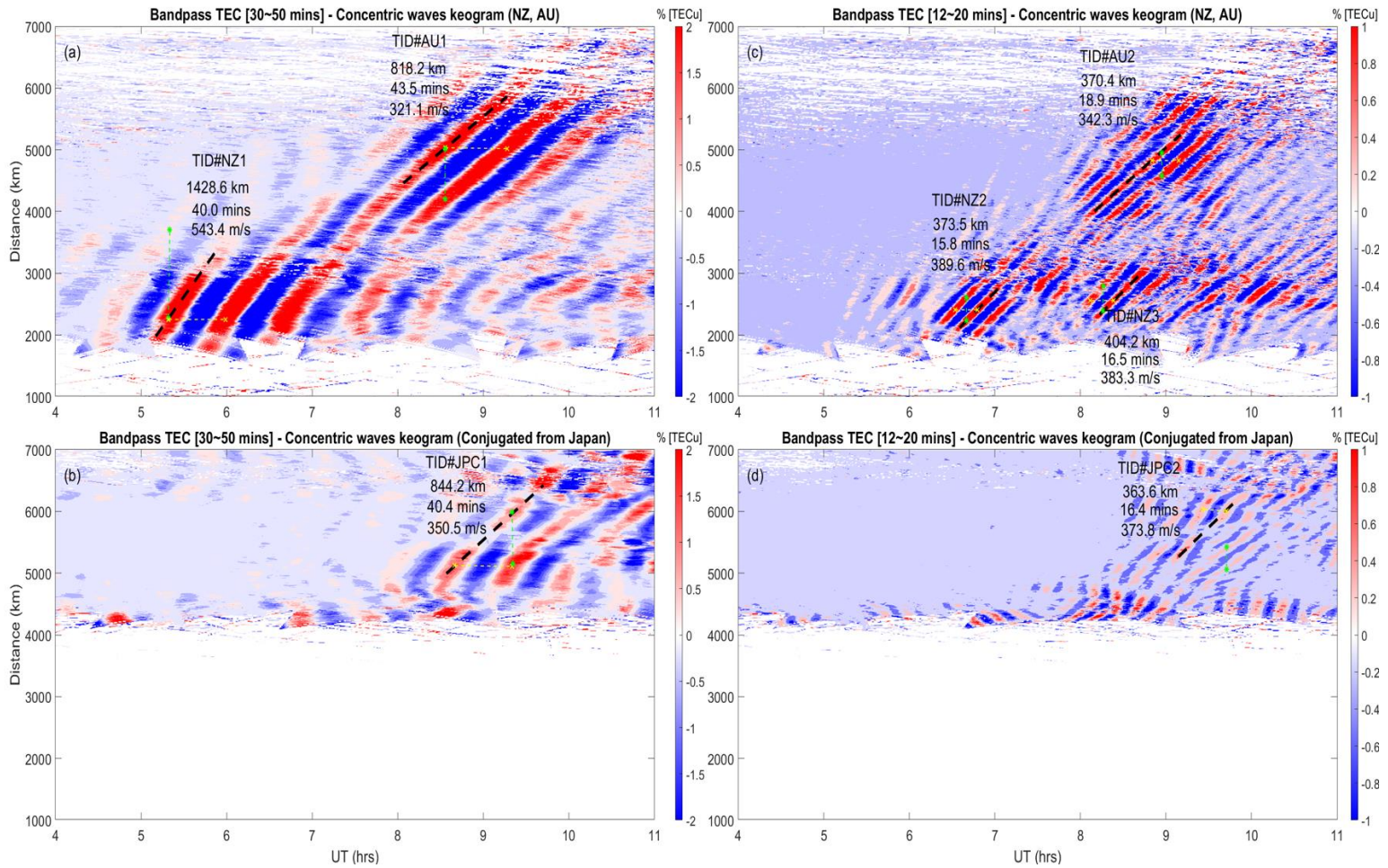


486
 487 Figure 1. (a)-(d) Bandpass filtered TECs of 30-50 min periods showing the conjugate concentric TIDs after
 488 mapping Japan (Australia) TECs to Sothern (Northern hemisphere), (e)-(h) with bandpass filter of 12-20
 489 min. The original TECs are plotted with “parula” colormap consisting of blue, green and yellow, while
 490 the conjugate TECs are plotted with “copper” colormap consisting of black and gold color.

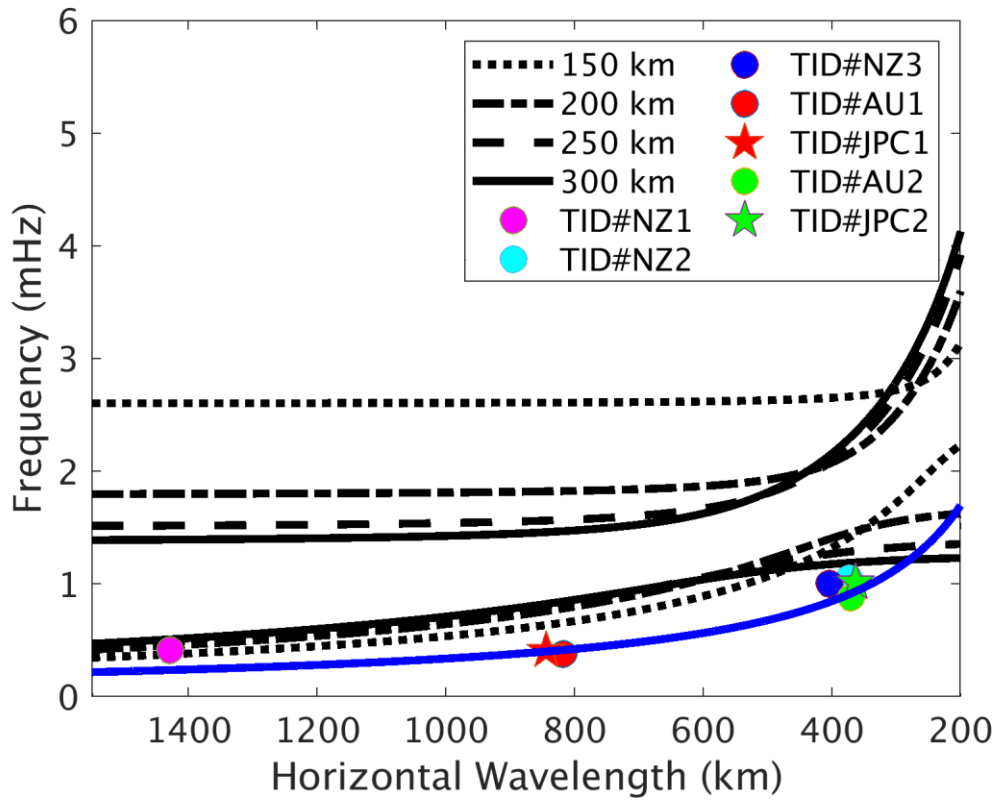


491

492 Figure 2. Hilbert Huang Transform of the TECs from Australia (top) and Japan (bottom) indicating the
 493 amplitude intensification after the eruption are manifest for frequency < 2 mHz (or 500s). The amplitude
 494 intensifications around 0800-1000UT for both regions suggest the conjugate effect. The minimum
 495 frequency in the vertical axes is set at 0.25 mHz (or 3600s).



496
 497 Figure 3. Keograms of the filtered TEC of 30-50 min (left) and 12-20 min (right) show the wave
 498 characteristics of CTIDs after 0400UT over New Zealand-Australia in (a) and (c), as the southern
 499 hemisphere conjugate locations of Japan are shown in (b) and (d). The distances are from the volcano to
 500 the sub-ionospheric point (SIP) locations over New Zealand and Australia areas, as observations over
 501 Japan have been mapped to the southern hemisphere.



502
 503 Figure 4. The theoretical dispersion curves of acoustic and gravity modes at 150 (dotted), 200 (dashed), 250
 504 (long-dashed) and 300 (solid) km altitudes are indicated in line plots. The colored dots/asterisk
 505 correspond to the observed TIDs shown in Figure 3. Blue solid line indicates the Lamb mode.

1
2
3
4
5
6
7
8
9
10
11
12
13
14
15
16
17
18
19
20
21
22
23
24

Geophysical Research Letters

Supporting Information for

Rapid Conjugate Appearance of the Giant Ionospheric Lamb Wave in the Northern Hemisphere After Hunga Tonga Volcano Eruptions

Jia-Ting Lin¹, Panthalingal K. Rajesh¹, Charles C. H. Lin¹, Min-Yang Chou^{2,3}, Jann-Yenq Liu^{4,5}, Jia Yue^{2,3}, Ho-Fang Tsai¹, Hoi-Man Chao¹ and Mu-Min Kung¹

¹Department of Earth Sciences, National Cheng Kung University, Taiwan

²NASA Goddard Space Flight Center, Community Coordinated Modeling Center, Greenbelt, MD, USA

³Physics Department, Catholic University of America, Washington, DC, USA

⁴Center for Astronautical Physics and Engineering, National Central University, Taiwan

⁵Department of Space Science and Engineering, National Central University, Taiwan

Contents of this file

Figures S2 to S3

Additional Supporting Information (Files uploaded separately)

Captions for Movie S1

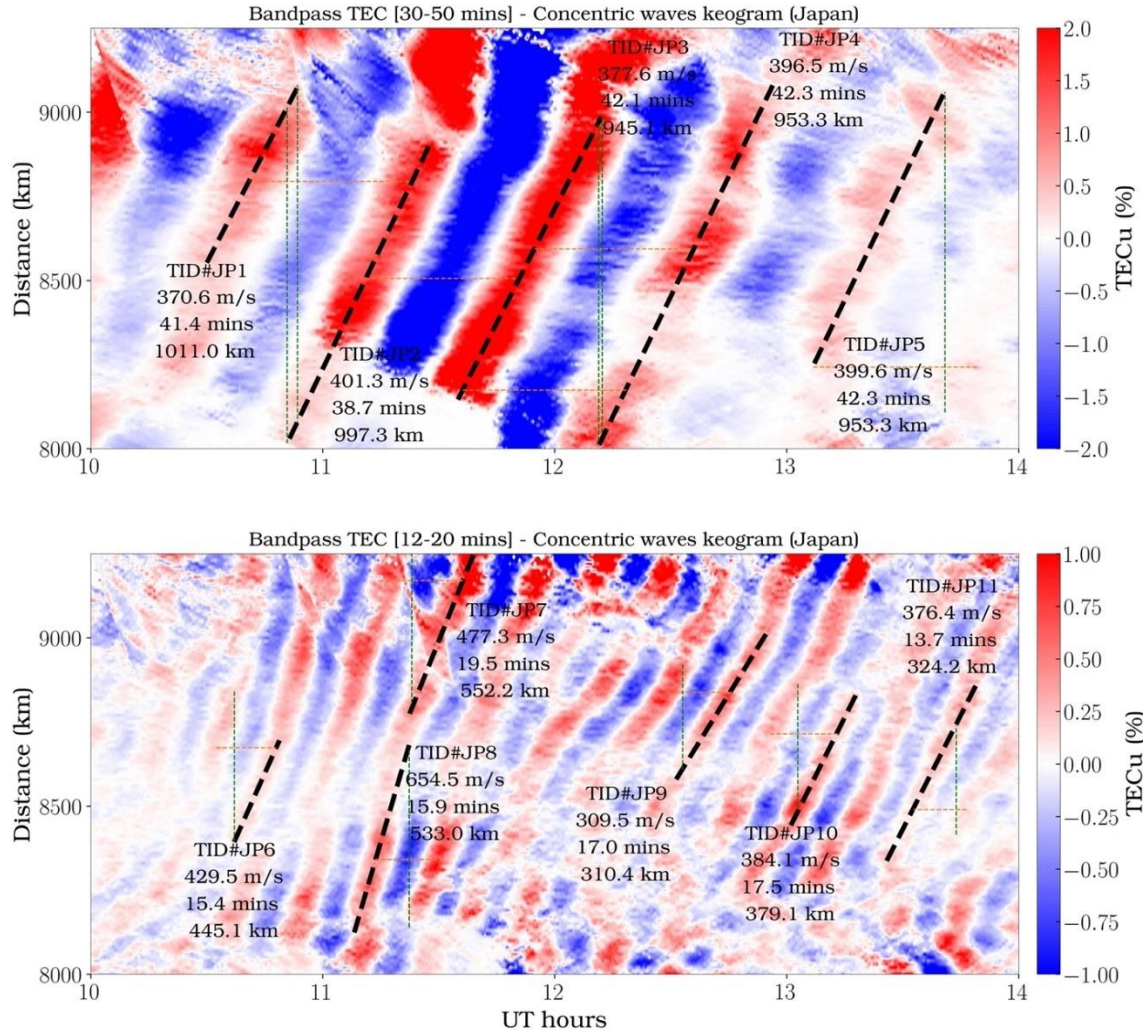
25 **Introduction**

26 The atmospheric pressure waves generated by Tonga volcano eruption triggered CTIDs in the
27 ionosphere, which are imaged by using TEC observations from the dense GNSS network over
28 Australia, New Zealand and Japan. The perturbations components of different wave
29 characteristics are separated by applying bandpass filters of 30-50 min, 12-20 min and 10-60
30 min periods. The movie S1 shows the complete time sequence of CTID's that arrive over New
31 Zealand, Australia, and Japan using the filtered TECs, offering a comprehensive view of their
32 time evolution and propagation depicted by the selected snapshots in Figure1.

33 One of the remarkable features seen in these observations are the conjugate CTIDs over Japan,
34 seen almost instantaneously after the arrival of the Lamb waves, but much ahead of their
35 anticipated arrival at Japan. Later, after 1000 UT, when the Lamb waves arrive over Japan, in
36 situ CTID's are observed in the TEC perturbations, similar to those seen in the conjugate
37 projections 0800-0900 UT in Figure 1. The Figure S2 shows these in situ perturbations over
38 Japan after 1000 UT, also showing their wave characteristics that match with the CTIDs
39 observed from the conjugate hemisphere.

40 Figure S3 shows the theoretical dispersion curve of acoustic and gravity modes in the
41 ionospheric heights and the surface Lamb mode. The wave characteristics of the CTIDs
42 extracted from Figure S2 are aligned with the Lamb mode, confirming that the CTID's are
43 driven by the volcano generated Lamb waves, similar to those shown in Figure 4.

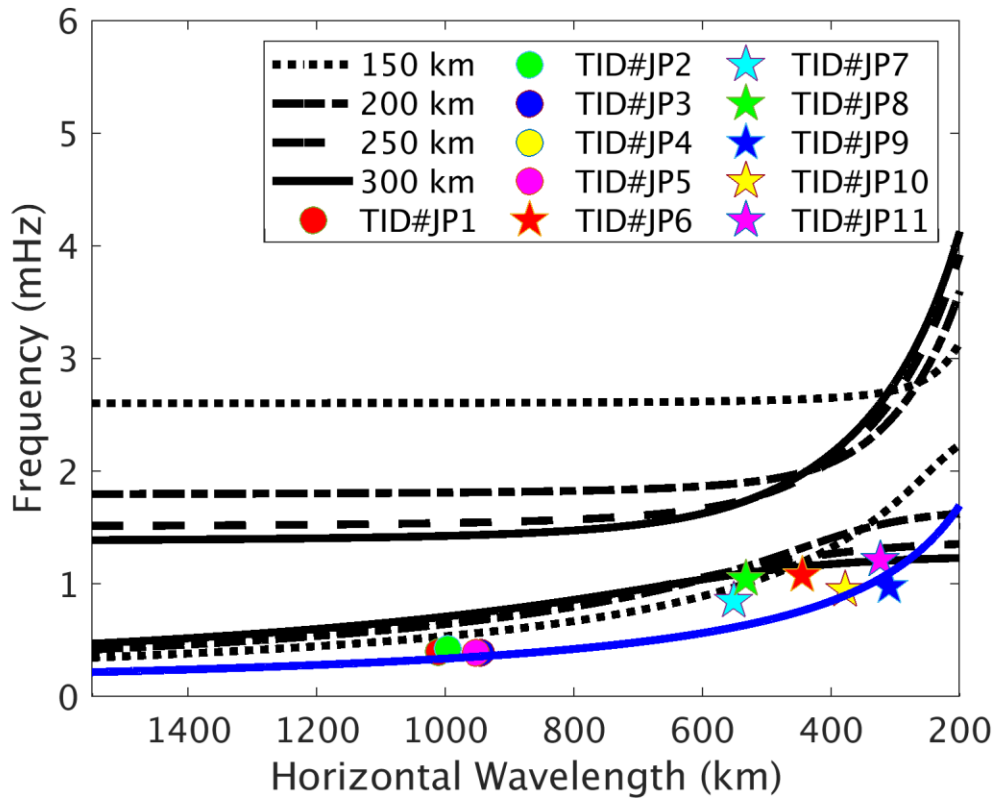
44



45

46 **Figure S2.** Keograms of the filtered TEC of 30-50 min (top) and 12-20 min (bottom) over Japan
 47 for the characteristics of CTIDs driven by the arrival of the air pressure Lamb wave to Japan at
 48 1000UT. The distances are from the volcano to the sub-ionospheric point (SIP) locations over
 49 Japan.

50



51

52 **Figure S3.** The theoretical dispersion curves of acoustic and gravity modes at 150 (dotted),
 53 200 (dashed), 250 (long-dashed) and 300 (solid) km altitudes over Japan region are indicated
 54 in line plots. The colored dots/asterisk correspond to the observed TIDs over Japan after 1000
 55 UT shown in Figure S2. Blue solid line indicates the Lamb mode.

56

57

58 **Movie S1.** Movie of bandpass filtered TECs of 12-20 min (left), 30-50 min (middle) and 10-60
 59 min (right) periods showing the conjugate concentric TIDs after mapping Japan (Australia)
 60 TECs to Southern (Northern hemisphere). The original TECs are plotted with "parula" colormap
 61 consisting of blue, green and yellow, while the conjugate TECs are plotted with "copper"
 62 colormap consisting of black and gold color. The dashed red circles denote the arrival of the
 63 atmospheric Lamb waves. The location of the eruption is marked using red star. The cyan line
 64 represents the locations of the geomagnetic equator, and the yellow and violet lines
 65 respectively indicate the locations $\pm 20^\circ$, and $\pm 40^\circ$ away from the equator.